Journal of Hazardous Materials

Waste plastics recycling for producing high-value carbon nanotubes: Investigation of the influence of Manganese content in Fe-based catalysts
--Manuscript Draft--

Corresponding Author:	Chunfei Wu, PhD Queen's University Belfast Belfast, UNITED KINGDOM
First Author:	Su He
Order of Authors:	Su He
	Yikai Xu
	Yeshui Zhang
	Steven Bell
	Chunfei Wu, PhD
Abstract:	Thermo-chemical conversion is a promising technology for the recycle of waste plastics, as it can produce high-value products such as carbon nanotubes (CNTs) and hydrogen. However, the low yield of CNTs is one of the challenges. In this work, the addition of Mn (0 wt.%, 1 wt.%, 5 wt.%, and 10 wt.%) to Fe-based catalyst to improve the production of CNTs has been investigated. Results show that the increase of Mn content from 0 wt.% to 10 wt.% significantly promotes CNTs yield formed on the catalyst from 23.4 wt.% to 32.9 wt.%. The results show that Fe-particles in the fresh catalysts are between 10-25 nm. And the addition of Mn in the Fe-based catalyst enhanced the metal-support interactions and the dispersion of metal particles, thus leading to the improved catalytic performance in relation to filamentous carbon growth. In addition, the graphitization of CNTs is promoted with the increase of Mn content. Overall, in terms of the quantity and quality of the produced CNTs, 5 wt.% of Mn in Fe-based catalyst shows the best catalytic performance, due to the further increase of Mn content from 5 wt.% to 10 wt.% led to a dramatic decrease of purity by 10 wt.%.

1 **Waste plastics recycling for producing high-value carbon nanotubes: Investigation of**
2 **the influence of Manganese content in Fe-based catalysts**
3 Su He[a], Yikai Xu[a], Yeshui Zhang[b], Steven Bell[a], Chunfei Wu[a]*

4 *[a] School of Chemistry and Chemical Engineering, Queen's University Belfast, Belfast, BT7*
5 *1NN, UK*
6 *[b] Electrochemical Innovation Lab (EIL), Department of Chemical Engineering, University*
7 *College London, London, WC1E 7JE, UK*
8 ** Corresponding authors: E-mail: c.wu@qub.ac.uk (C. Wu)*

9 **Abstract**

10 Thermo-chemical conversion is a promising technology for the recycle of waste plastics, as it
11 can produce high-value products such as carbon nanotubes (CNTs) and hydrogen. However,
12 the low yield of CNTs is one of the challenges. In this work, the addition of Mn (0 wt.%, 1
13 wt.%, 5 wt.%, and 10 wt.%) to Fe-based catalyst to improve the production of CNTs has been
14 investigated. Results show that the increase of Mn content from 0 wt.% to 10 wt.% significantly
15 promotes CNTs yield formed on the catalyst from 23.4 wt.% to 32.9 wt.%. The results show
16 that Fe-particles in the fresh catalysts are between 10-25 nm. And the addition of Mn in the Fe-
17 based catalyst enhanced the metal-support interactions and the dispersion of metal particles,
18 thus leading to the improved catalytic performance in relation to filamentous carbon growth. In
19 addition, the graphitization of CNTs is promoted with the increase of Mn content. Overall, in
20 terms of the quantity and quality of the produced CNTs, 5 wt.% of Mn in Fe-based catalyst
21 shows the best catalytic performance, due to the further increase of Mn content from 5 wt.% to
22 10 wt.% led to a dramatic decrease of purity by 10 wt.%.

24 Keywords: Waste plastics; carbon nanotubes; Mn-catalyst; thermo-chemical processing;
25 pyrolysis

1. Introduction

Nowdays, plastics are used in various aspects, from household goods such as packaging, clothing, electrical devices, to industrial applications such as automotive parts and insulations (Lettieri and Al-Salem, 2011). The vast demand for plastic results in increasing plastic production year by year. In 2016, plastic production reached 330 million tons and will double within the next 20 years under the current estimationed growth rate (Lebreton and Andrady, 2019). The extensive use of plastics generates a large amunt of wastes. These waste plastics cause severe environmental pollution if they were not well managed. The general methods for plastics waste management include landfill, energy recovery and recycling. Landfill is the most common method for plastic waste treatment in developing countries due to the cheap cost. Even in Europe, ~31 % of waste plastics still goes to land fill, wasting energy stored in the plastic and also causing severe environmental challenges (Drzyzga and Prieto, 2019; Lebreton and Andrady, 2019). In pricinple, recycling of plastic waste provides a more economical and environmental-friendly solution. However, current state of the art technologies of plastic wastes recycling mostly produce low-value products, such as cricks and road construction materials. Therefore, converting waste plastics into high-value products such as carbon nanotubes (CNTs) is a promising alternative for plastic waste management.

Since its discovery by Iijima in 1991 (Iijima, 1991), the extraordinary mechanical and electrical properties of CNTs have allowed it to find a variety of potential applications, such as drug delivery (Bianco et al., 2005), energy storage (Landi et al., 2009), materials strengthening (Andrews et al., 2002), etc. As a result, CNTs production from catalytic pyrolysis of plastic waste has been obtaining increasing interest. The key component to plastic pyrolysis is the catalyst which determins both the yield and quality of the produced CNTs.

In the chemical vapour deposition (CVD) synthesis of CNTs from various carbon feedstocks, Fe, Co and Ni are the most effective and widely used catalysts (Shah and Tali, 2016). The using of different catalysts could lead to the different properties and yield of CNTs. Lee et al. investigated the influence of Fe, Co and Ni-silica supported catalysts and reported that Fe catalyst resulted in the best crystallinity of produced CNTs. Sivakumar et al. reported that the produced CNTs over Ni catalyst have higher thermal stability than Fe catalyst (Sivakumar et al., 2011). In addition, the morphology and quality of the produced CNTs were also strongly affected by carbon feedstocks (Yan et al., 2015). In the catalytic synthesis of CNTs using plastic as carbon source, extensive researches have also been conducted on a range of metals e.g. Fe (Wu et al., 2017a), Ni (Yao et al., 2018) and Co (Acomb et al., 2016). Acomb et al. produced CNTs using Fe/Al_2O_3 catalyst from catalytic pyrolysis of LDPE (Low-Density Polyethylene) and obtained carbon deposition yielded 26 wt.% (Acomb et al., 2016). Yao et al. reported using $Fe/\alpha-Al_2O_3$ and $Fe/\gamma-Al_2O_3$ catalyst to produce CNTs from real world plastics, and the carbon yielded 35.2 and 32.6 wt.%, respectively (Yao et al., 2018). In Wu et al's work, Fe/SiO_2 catalysts were used to produce CNTs with carbon yield 29 wt.% from PP(Wu et al., 2017a). In the previous work, compared to Ni or Co based catalyst, Fe-based catalysts lead to a higher yield of carbon from catalytic conversion of plastics, which is owing to the higher carbon solubility and higher carbon diffusion rate of iron nanoparticles (Deck and Vecchio, 2006) as well as the appropriate strength of metal-support interactions (Acomb et al., 2016).

Mn acting as an effective promoter was used in a variety catalytic reactions, such as the

70 Fischer–Tropsch process (Bezemer et al., 2006; Ding et al., 2013; Xu et al., 2013a; Zhao et al.,
71 2012), volatile organic compounds oxidation (Tang et al., 2014), and the decomposition of
72 nitrous oxides (Jia et al., 2016; Karásková et al., 2010). As for the synthesis of CNTs, Mn as a
73 promoter in Ni-based and Co-based catalysts have also been reported from various carbon
74 feedstocks (Zein and Mohamed, 2004)(Nahil et al., 2015)(Wu et al., 2017b). The promoting
75 effects of Mn in Ni-based catalyst for CNTs synthesis from methane were reported by several
76 researchers. For example, Zein et. al reported Mn-Ni/TiO$_2$ catalysts prepared by three different
77 methods for the production of hydrogen and CNTs from methane (Zein and Mohamed, 2004).
78 However, only a fixed content of Mn (15 wt.%) was used in the research, and the reasons for
79 the catalytic performance was not clear. Ran et. al further investigated the doping effect of Mn
80 on CNTs formation in the presence of Ni/MgO catalysts with varied Mn content. It was found
81 that the addition of Mn to the Ni/MgO catalyst significantly increased the carbon yield, with
82 the highest carbon yield produced by the catalyst with Mn:Ni a molar ratio of 0.2:1 (Ran et al.,
83 2014). In addition, Becker et al. reported that Mn-Co catalysts with Mn:Co molar ratio of 1:1
84 led to the highest CNTs yield using ethene as carbon source (Becker et al., 2011). He et. al
85 applied Mn-Fe/MgO catalyst to improve the chirality distribution of the produced single-walled
86 CNTs using CO as carbon source (He et al., 2016).

87 Mn's promoting effects have also been investigated in the CNTs synthesis from waste
88 plastics. In Nahil et. al's work, a variety of metals (Zn, Mg, Ca, Ce, Mo, Mn, etc.) added into
89 Ni-based catalysts have been investigated for the catalytic conversion of waste plastics
90 (polypropylene) into CNTs (Nahil et al., 2015). It was found that the addition of Mn into Ni-
91 based catalyst resulted in the highest yield of CNTs. Further work by Wu et al. investigated the
92 effects of Mn content on CNTs synthesis in the Ni-based catalyst. The Mn-Ni/Al$_2$O$_3$ catalyst
93 with Mn:Ni a molar ratio of 2:2 produced a higher yield of carbon compared to Mn:Ni with a
94 molar ratio of 2:1 in the synthesis of CNTs using waste plastics (polypropylene) as carbon
95 feedstock.

96 Owing to the great catalytic performance of Fe-based catalyst and Mn as a promising
97 promoter in CNTs formation from plastics, there is a potential of further increasing CNTs
98 production and quality by doping Mn into Fe-based catalyst during catalytic conversion of
99 waste plastics. Therefore, in this work, we report the influence of Mn content in the Fe-based
100 catalyst for CNTs production from catalytic pyrolysis of waste plastics. This work aims to
101 optimise the development of Fe-based catalysts by adding Mn in relation to CNTs production
102 from waste plastics.

103 **2. Experimental**

104 **2.1 Materials and preparation of catalyst**

105 The plastic raw material used in this study was recycled polypropylene (PP) pellet
106 obtained from regain polymer Ltd. with a diameter of ~2mm. The chemicals
107 Mn(NO$_3$)$_2$•H$_2$O (98%, Sigma-Aldrich, cat. no. 288640), ~~Al$_2$O$_3$ (≥98%, puriss, Sigma-~~
108 ~~Aldrich, cat. no. 11028)~~ and Fe(NO$_3$)$_3$•9H$_2$O (≥98%, ACS reagent, Sigma-Aldrich, cat.
109 no. 16828) were used as starting materials. Al$_2$O$_3$ (≥98%, puriss, Sigma-Aldrich, cat.
110 no. 11028) with particle size around 10 μm is used as the catalyst support. All materials
111 were used directly without any pre-treatment. MnFe/Al$_2$O$_3$ catalysts were prepared by

112   a wet impregnation method. The catalysts contain 10 wt.% of Fe. The content of Mn is
113   0 wt.%, 1 wt.%, 5 wt.% and 10 wt.%, respectively. And the corresponding catalyst is
114   assigned as 0Mn10Fe, 1Mn10Fe, 5Mn10Fe and 10Mn10Fe, respectively. For
115   comparison, a catalyst with 10 wt.% Mn without Fe (10Mn0Fe) was prepared use the
116   same method.

117   During catalyst preparation, the required amount of $Mn(NO_3)_2 \cdot xH_2O$ and $Fe(NO_3)_3 \cdot 9H_2O$
118   were dissolved in 100 ml of deionized water, and the mixture solution was stirred for ~0.5 h
119   until the chemicals were fully dissolved. The required amount of Al_2O_3 was then slowly added
120   into the mixture solution and stirred for ~1 h. After that, water was removed by evaporation at
121   90 °C, followed by drying in an oven at 105 °C overnight to remove the remaining water.
122   Finally, the dried catalyst precursors were grounded into a fine powder and then were heated
123   in the air atmosphere at a heating rate of 10 °C min^{-1} to 500 °C for 3 h of calcination.

124   **2.2 Catalytic pyrolysis of plastic waste into CNTs**

125   The catalytic pyrolysis of plastic waste into CNTs was performed in a two-stage reactor in
126   this study. Fig. 1 shows the schematic diagram of this reaction system. The first-stage reactor
127   consists of a horizontal quartz tube placed in a tubular furnace for PP pyrolysis. The generated
128   vapor was carried by N_2 with a flow rate of 100 ml min^{-1} and after condensation, the non-
129   condensed products passed through the second-stage of the reactor.

130   For each run of the experiment, 2 g of PP was located inside an aluminium boat in the centre
131   of the first-stage reactor, and 0.5 g of catalyst supported by ~30 mg of quartz wool was located
132   in the centre of the second-stage reactor. The reaction system was purged by N_2 for ~10 min
133   before the second-stage reactor started to heat from room temperature to 800 °C with a heating
134   rate of 40 °C min^{-1}. When the second-stage reactor reached the set point temperature, the first-
135   stage reactor containing 2 g of PP started to heat from room temperature to 200 °C with a
136   heating rate of 40 °C min^{-1}, followed by heating from 200 °C to 500 °C with a heating rate of
137   10 °C min^{-1}. After ~1 h of reaction time, the reaction system was slowly cooled down to room
138   temperature under N_2 protection, and the reacted catalyst together with the produced CNTs
139   were collected for further characterisations. The Fe-based catalysts with different Mn contents
140   associated with the production of CNTs were studied.
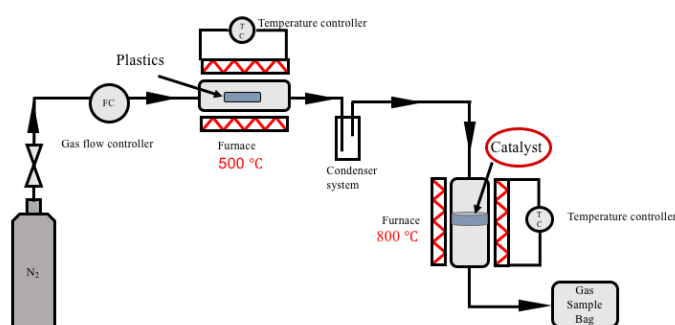
141

142   **Fig. 1.** Schematic diagram of the two-stage reaction system.

143   **2.3 Characterisation of fresh and reacted catalyst**

144   TA Instruments TGA 2950 thermogravimetric analyser (TGA) was used to analyse the
145   temperature programme reduction (TPR) of the fresh catalyst to observe the reduction of the
146   catalyst metal. Under a mixed gas of H_2 and N_2 gas (5 vol.% : 95 vol.%), ~50 mg of catalyst
147   was heated from room temperature to 100 °C at a heating rate of 10 °C min^{-1} and held for 10
148   min, then the temperature increased to 950 °C under at the same heating rate to record the TPR
149   curve.
150   Temperature programme oxidation (TPO) analysis for the reacted catalysts was conducted
151   by the same TGA 2950 equipment using air gas to measure the amount of carbon formed on
152   the reacted catalyst and to distinguish different types of carbons, such as amorphous carbons or
153   graphite. For each TPO process, ~30 mg of reacted catalyst sample was heated to 800 °C in air
154   at a heating rate of 15 °C min^{-1}. The fresh and reacted catalysts were also characterized by a
155   Panalytical X-ray diffraction (XRD) equipment with a scanning step of 0.033° using
156   Cu•kα1 radiation in the range from 5° to 80° and the data was analysed with Highscore software.
157   The strongest peak was chosen to calculate the crystallite size by Scherrer equation. The surface
158   morphology and diameter of the metal particles of the catalysts were observed with a FEI
159   Quanta FEG Oxford Ex-ACT scanning electron microscope (SEM) and a Jeol 2100 LaB6
160   transmission electron microscope (TEM). The WITec Alpha 300R Confocal Raman
161   Microscope equipped with a 532 nm diode laser with an output power of 30 mWwas used to
162   perform Raman spectroscopic analysis of the reacted catalyst.

163   **3. Results and discussion**

164   **3.1 Characterization of fresh catalysts**

165   XRD results of the prepared Fe-based catalysts with varied Mn contents are shown in Fig. 2.
166   In general, the diffraction patterns of all four catalysts are dominated by the characteristic peaks
167   of α-Fe_2O_3 at 4.2°, 33.3°, 35.7°, 41.05°, 49.71°, 54.36°, 62.74°, 64.30° 2θ, indicating that the
168   main composition of the catalysts are α-Fe_2O_3. For the 0Mn10Fe catalyst, the diffraction
169   patterns only consist of peaks corresponding to α-Fe_2O_3 and Al_2O_3. For the Mn-doped catalysts,
170   the XRD data show weak diffraction of manganese oxides, which is in good agreement with
171   literatures (Feyzi and Jafari, 2012; Lee et al., 1991; Nasser et al., 2018; Yang et al., 2005). This
172   might be due to Mn was present as amorphous or highly dispersed on the surface of the Al_2O_3
173   support (Nasser et al., 2018).
174   The size of the α-Fe_2O_3 crystallite phase was calculated using the Scherrer equation. For the
175   0Mn10Fe catalyst, the crystallite size is 107.1 nm. Interestingly, it is found that the crystallite
176   size of 1Mn10Fe, 5Mn10Fe and 10Mn10Fe catalyst are much smaller, at 14.0 nm, 8.4 nm, and
177   30.3 nm, respectively. It is indicated that an appropriate amount of Mn dopant could
178   significantly improve the dispersion of iron in the catalyst. The crystallite size of the 10Mn10Fe
179   catalyst is larger than the 5Mn10Fe catalyst, which could be resulted from the excessive amount
180   of Mn dopant in the catalyst. It is now well-established that the size of the catalyst particles are
181   crucial for CNTs formation and that larger particles often exhibit lower catalytic activities due
182   to the reduced active-surface area (Acomb et al., 2016; Liu et al., 2009). Therefore, the above
183   findings demonstrate that an appropriate amount of Mn is required to be added to the Fe-based

184 catalyst in terms of the catalytic conversion of waste platics to form CNTs.
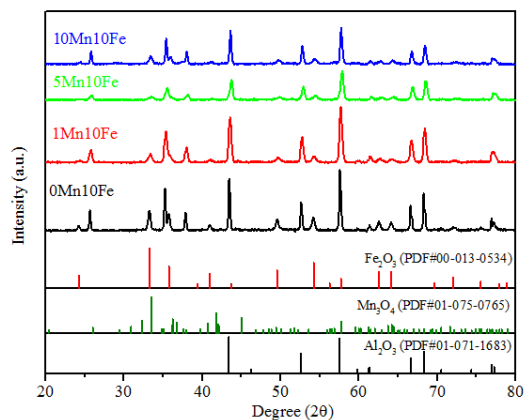
185
186
187 **Fig. 2**. X-ray diffraction of the freshFe-based catalysts with different amount of (Mn
188 0Mn10Fe, 1MnFe, 5Mn10Fe and 10Mn10Fe).
189

190 The H_2-TPR results for the four catalysts are shown in Fig. 3. Several reduction peaks are
191 obtained since both Fe and Mn elements possess several types of oxide forms and the reduction
192 of Fe_2O_3 and Mn_3O_4 proceed subsequentially. Hydrogen reduction of Fe_2O_3 involves two or
193 three steps according to different reduction temperatures (Pineau et al., 2006): when the
194 reduction temperature is below 570 °C, wüstite FeO was formed as an intermediate product
195 before the formation of Fe, as illustrated in Eq. (1); when the reduction temperature is above
196 570 °C, Fe_2O_3 reduced into Fe_3O_4 and then directly reduced into Fe, as shown in Eq. (2):
197 $Fe_2O_3 \rightarrow Fe_3O_4 \rightarrow FeO \rightarrow Fe$ (1)

198 $Fe_2O_3 \rightarrow Fe_3O_4 \rightarrow Fe$ (2)
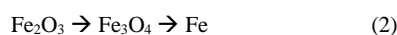
199 As indicated in Fig. 3, the 0Mn10Fe catalyst undergoes two stages of reduction. ~0.68 wt.%
200 weight loss occurred in the first stage and ~5.5 wt.% weight loss occurred in the second stage.
201 The first reduction peak at 420 °C can be attributed to the reduction of α-Fe_2O_3 to Fe_3O_4. The
202 second broad peak as illustrated in the range of 450-750 °C can be attributed to the
203 subsequentially reduction of Fe_3O_4 to FeO and Fe following Eq.(1) process. 1Mn10Fe have
204 three reduction stages, which have a weight loss of 0.47 wt.%, 0.69 wt.% and 2.47 wt.%,
205 respectively. 1Mn10Fe shows a major reduction peak in the first stage for the reduction of α-
206 Fe_2O_3 to Fe_3O_4 which shifted towards higher temperature compared to 0Mn10Fe. Meanwhile,
207 the first stage weight loss for 1Mn10Fe is lower than that compared to 0Mn10Fe. These
208 suggesting that the Mn-doped catalyst is more resistant to the reduction and the metal-support
209 interactions is enhanced with the addition of Mn. The new peak appearring at 540 °C for
210 1Mn10Fe catalyst indicates that the reduction of Fe_3O_4 to Fe via FeO is further stabilized by
211 MnO (Leith and Howden, 1988; Yang et al., 2005, 2004).The weight loss of four reduction
212 stages for the 5Mn10Fe catalyst are 0.58 wt.%, 0.61 wt.%, 0.92 wt.% and 2.4 wt.%, respectively.
213 And the 10Mn10Fe catalyst showes an obvious increase of weight loss in the first two reduction

214   peaks, which are 1.4 wt.% and 1.3 wt.%. respectively. For the third and fourth reduction stages,
215   it shows a similar weight loss value compared to the 1Mn10Fe and 5Mn10Fe catalysts. The
216   new reduction peak appears at ~370 °C for the 5Mn10Fe and 10Mn10Fe catalysts can be
217   attirbuted to the large amount of Mn_3O_4 which is reduced into Mn with MnO as intermediates.
218   This indicates the overall weight loss is increased from 3.63 wt.% to 6.1 wt.% when the Mn
219   content increases from 1 wt.% to 10 wt.% in the catalyst, but the corresponding reduction
220   weight loss for Fe_3O_4 is similar. In addition, the major α-Fe_2O_3 reduction peak for the 5Mn10Fe
221   and 10Mn10Fe catalysts shifts towards higher temperature at ~430 °C compared to the
222   1Mn10Fe catalyst, suggesting that increasing the Mn loading from 0-5 wt.% improves the
223   metal-support interactions but the further increase of Mn loading to 10 wt.% has slight impacts
224   on the metal-support interaction.
225

(a)   (b)
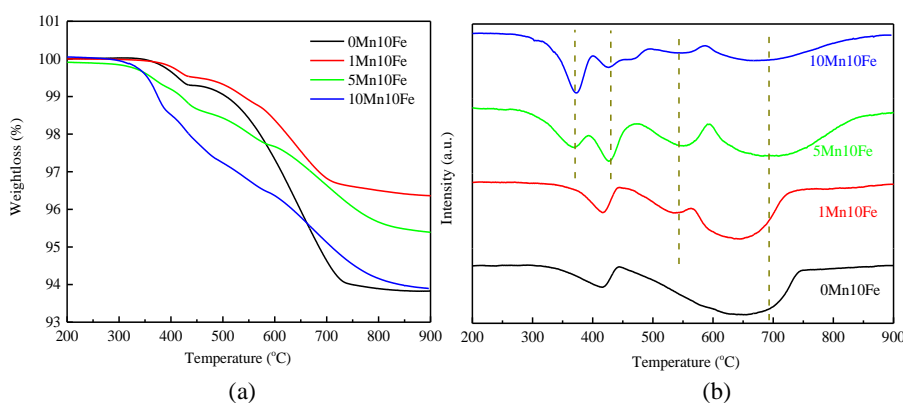
226   **Fig. 3.** TPR (a) and DTG-TPR (b) profiles of the fresh Fe-based catalysts with varied amount
227   of Mn in the catalysts (0Mn10Fe, 1MnFe, 5Mn10Fe and 10Mn10Fe).

228   **3.2 The production of CNTs**

229   **3.2.1 Temperature programmed oxidation (TPO) of the reacted catalysts**

230   TPO results of the reacted catalysts (0Mn10Fe, 1MnFe, 5Mn10Fe and 10Mn10Fe) are shown
231   in Fig.4. Based on previous work, the weight loss of amorphous carbons and filamentous
232   carbons can be distinguished using oxidation temperature due to their different oxidation
233   properties: the weight loss occurred before 600 °C corresponds to the oxidation of amorphous
234   carbon, while the weight loss occured after 600 °C is related to the oxidation of filamentous
235   carbon (assumed as CNTs in this study) (Wu and Williams, 2009; Yang et al., 2015; Zhang et
236   al., 2017). From Fig. 4(a), a slight increase of the catalyst weight between 350 and 500 °C is
237   observed due to the oxidation of Mn and Fe. For the reacted 10Mn0Fe catalyst, no weight loss
238   is observed, which indicates that almost no carbons are deposited on the surface of the reacted
239   catalyst. Therefore, it is demonstrated that the 10Mn0Fe catalyst without Fe is inactive for
240   carbon formation. However, the remaining four Fe-based catalysts show a significantly increase
241   of weight loss with increasing Mn content and the 10Mn10Fe catalyst gives the highest carbon
242   formation (~41.5 wt.% of the total catalyst), as shown in Fig.4(a). It is indicated that Fe is the

243   active sites and Mn promotes the catalytic conversion of waste PP to form carbon. Other

244   researchers have obtained similar results, that is, Mn acted as a promoter for the production of

245   CNTs in Ni-based (Ran et al., 2014; Zein and Mohamed, 2004) and Co-based catalysts (Becker

246   et al., 2011).

247   The yield of amorphous and filamentous carbons are determined by the TGA-TPO curves

248   according to their different oxidation temperatures/thermal stabilities. The carbon yield of

249   amorphous and filamentous carbons for each catalyst is obtained according to Eq.(3). This is

250   calculated based on the weight loss of each reacted catalysts on TGA-TPO results as shown in

251   Fig. 4. And the calculation results are shown in Fig. 5(a).

252 $$m_i = \frac{w_i}{M} \times 100\% \tag{3}$$

253   Where 'i' means amorphous or filamentous carbons. The 'w_i' represents the weight of

254   amorphous or filamentous carbons deposited on the surface of reacted, 'M' represents the mass

255   of reacted catalyst, and 'm_i' means the yield of amorphous or filamentous carbons, respectively.

256 **Fig. 4.** TGA-TPO (a) and DTG-TPO (b) patterns of reacted catalyst with different amount of

(a)
(b)
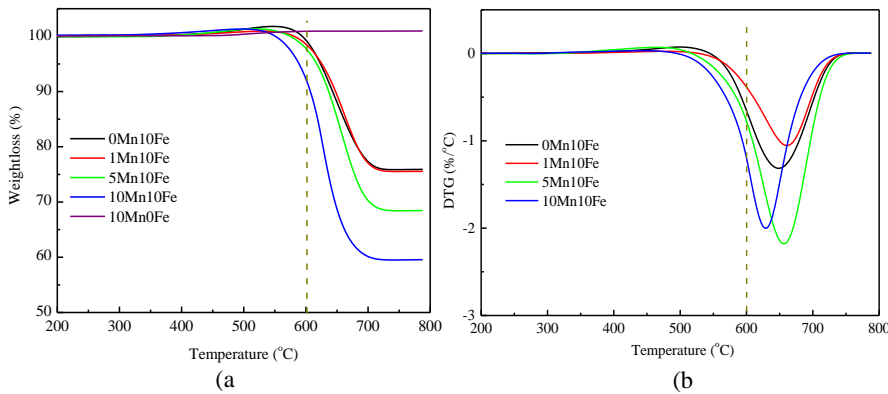
257 Mn addition in the catalysts (0Mn10Fe, 1MnFe, 5Mn10Fe, 10Mn10Fe and 10Mn0Fe).

258

259   As shown in Fig. 5(a), the addition of 1 wt.% of Mn into Fe-based catalyst shows slight

260   increase on carbon content. A further increase of Mn to 5 wt.% and 10 wt.% results in a

261   significantly incrase of both amorphous and filamentous carbons. It is worth noting that when

262   the Mn content is increased from 1 wt.% to 5 wt.%, the yield of filamentous carbons

263   significantly increases by ~6 wt.%. However, as shown in Fig. 5, when the Mn content is further

264   increased from 5 wt.% to 10 wt.%, the yield of filamentous carbon is only increased by ~2.5

265   wt.% while amorphous carbon increases by ~5 wt.%.

266   The mass ratio between amorphous and filamentous carbons for different catalysts is

267   calculated according to Eq.(4) based on the carbon yield calculated from Eq.(3), and the

268   calculation results are shown in Fig. 5(b).

269 $$M_i(\%) = \frac{m_i}{\sum m_i} \times 100\% \tag{4}$$

270   Where the 'M_i' mean the mass ratio of filamentous and amorphous carbon.

271   As shown in Fig. 5(b), the mass ratios of amorphous and filamentous carbons generated on

272   the 0Mn10Fe, 1Mn10Fe and 5Mn10Fe catalysts are similar. However, when the Mn content
273   reaches 10 wt.%, the mass ratio of unwanted amorphous carbons is significantly increased to
274   20.9 wt.%. Although increasing the addition of Mn from 0-10 wt.% promotes carbon formation
275   for both filamentous and armophous carbons as shown in Fig. 5(a), to some extent, the influence
276   of Mn addition on the mass ratio of filamentous and armophous carbons is different. The
277   addition of Mn in the range of 0-5 wt.% shows less influence on the mass ratio of produced
278   filamentous carbons while a further addition of Mn to 10 wt.% dramatically reduces the mass
279   ratio of filamentous carbons. It is suggested that the addition of Mn in the range of 0-5 wt.%
280   promotes CNTs growth and the further increase of Mn content favours the formation of
281   amorphous carbons. In addition, the DTG-TPO results in Fig.4(b) show that the oxidation peak
282   for the 10Mn10Fe catalyst occures at lower temperature compared to 0Mn10Fe, 1Mn10Fe and
283   5Mn10Fe. It is indicated that a lower oxidation peak is corresponding to a higher mass ratio of
284   amorphous carbons.
285
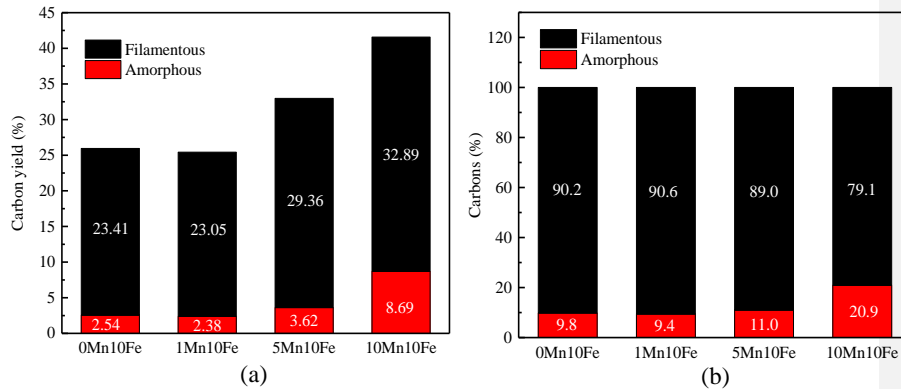
286   **Fig. 5.** (a) Amorphous/filamentous carbon yield on each of the reacted catalysts. (b) Mass
287   ratio of amorphous and filamentous carbons on each catalyst.

288   **3.2.2 X-ray diffraction (XRD) of reacted catalysts**

289   Fig. 6 shows the XRD patterns of the four reacted catalysts. The Fe crystallite size is obtained
290   from Scherrer equation. The results show that the Fe crystallite size of the four reacted catalysts
291   is quite similar, which are 14.5 nm, 19.9 nm, 19.9 nm, and 19.9 nm for the 0Mn10Fe, 1Mn10Fe,
292   5Mn10Fe and 10Mn10Fe catalyst, respectively. From Fig. 6, it can be seen that the four reacted
293   catalysts mainly contain iron carbides (Fe_3C and Fe_5C_2) and Fe phases after reaction, suggesting
294   that α-Fe_2O_3 was fully reduced to Fe by the generated gas and then the reduced Fe was partially
295   carbonised. Similar phase transformation of α-Fe_2O_3 to Fe_3C was also reported in the recent
296   study (Zhang et al., 2020). For the 5Mn10Fe and 10Mn10Fe catalysts, there are additional
297   peaks detected in the XRD patterns, indicating the existence of MnO phase. In addition, the
298   peak intensity of Fe_3C phase is decreased while the Fe_5C_2 intensity is increased with the
299   increase of Mn content in the Fe-based catalyst. It is suggested that Mn in the catalyst promote
300   the carburization of Fe_5C_2 rather than Fe_3C, hence, the carbon solubility per iron atom is

301 reduced. Similarly effects on hidering the carburization of Fe have also been reported (Lee et
302 al., 1991; Nasser et al., 2018; Xu et al., 2013b). The lower carbon content accelerated
303 intermediate carbides to reach the carbon concentration required for graphite precipitation,
304 hence to promote CNTs growth (Deck and Vecchio, 2006).
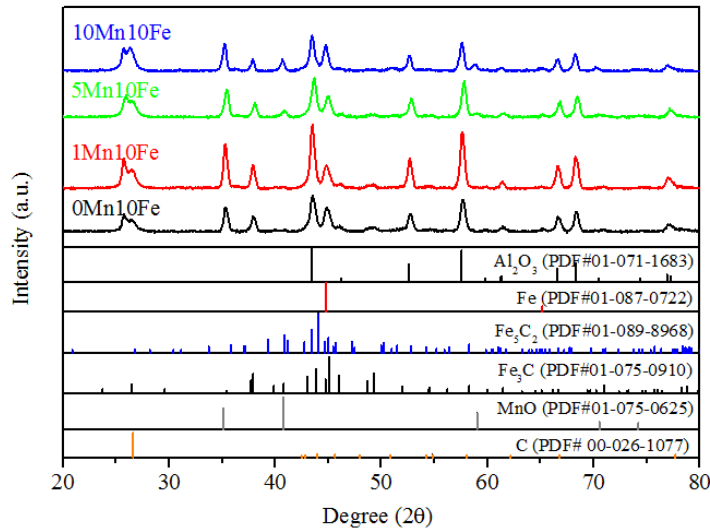
305

306 **Fig. 6.** X-ray diffraction of the reacted Fe-based catalysts contain Mn.

3.2.3 SEM and TEM results of the ~~reacted~~ catalysts

308   Fig. 7 shows the SEM results of the four fresh and reacted catalysts. It is indicated that the
309 overall particle of the fresh catalyst is around 10 μm. After catalytic conversion of waste
310 plastics, an aboundance of filamentous carbons could be clearly observed on the catalysts
311 surface. The morphologies of the formed filamentous carbons on the four reacted catalysts were
312 further investigated by TEM as shown in Fig. 8. The results illustrate the filamentous carbons
313 with different structures in terms of size and homogenousness are formed over the four catalysts.
314 Obviously, the metal particles are wrapped inside the tip of the CNTs, which is consistent with
315 the tip growth mechanism of CNTs (Amelinckx et al., 1994). The formed CNTs with
316 comparatively unsmooth and unhomogeneous structures are clearly observed for the 5Mn10Fe
317 and 10Mn10Fe catalysts. The CNTs produced by the four catalysts have similar inner diameters
318 (between 10-25 nm), which is consistent with the crystallite size of the active metal particles
319 (15-20 nm) within the catalysts calculated from XRD results. It is demonstrated that the size of
320 the CNTs is directly correlated to the particle size of active sites (Kotov et al., 2019)(Cheung
321 et al., 2002; Ding et al., 2004; Nerushev et al., 2003). Interestingly, adding Mn to Fe-based
322 catalysts seems to improve the radical growth of CNTs. As shown in Fig.8, the outer diameters
323 of CNTs produced by the 0Mn10Fe and 1Mn10Fe catalysts are similar, ranging from 15-60 nm,
324 while the outer diameter of CNTs formed on 5Mn10Fe and 10Mn10Fe catalysts are larger (30-
325 115 nm). This may be attributed to the Mn contents affected the supersaturation degree of
326 carbon atoms in the Fe nanoparticle as described in a recent study (Hayashi and Kohno, 2020).
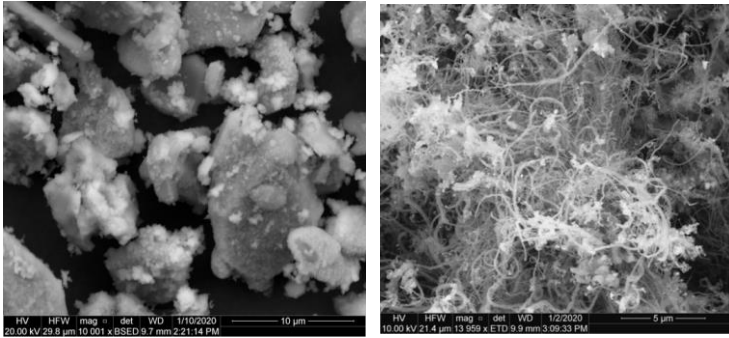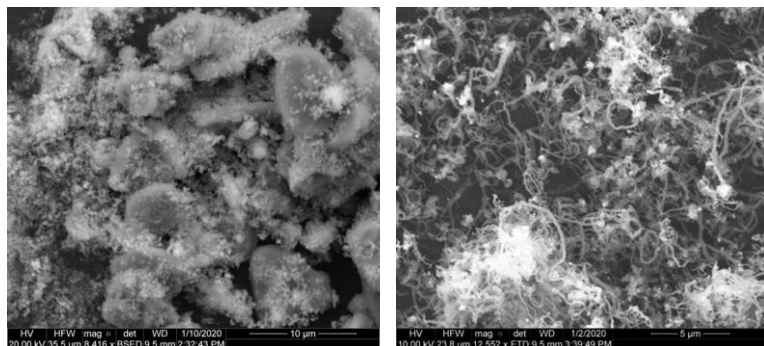
327
328
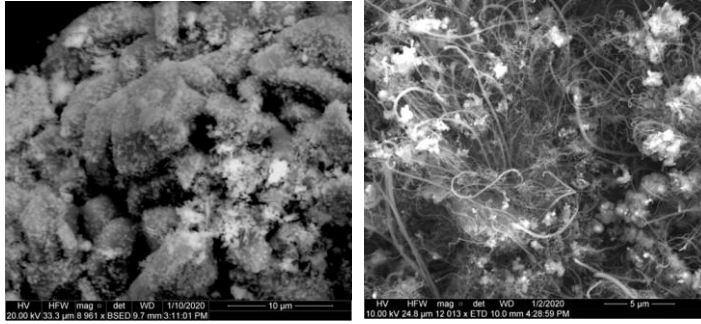
329
330
(a)0Mn10Fe
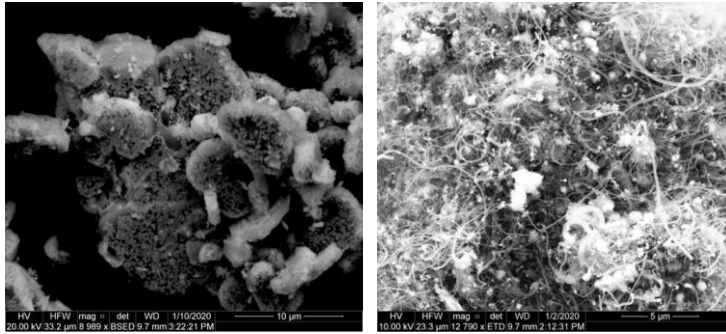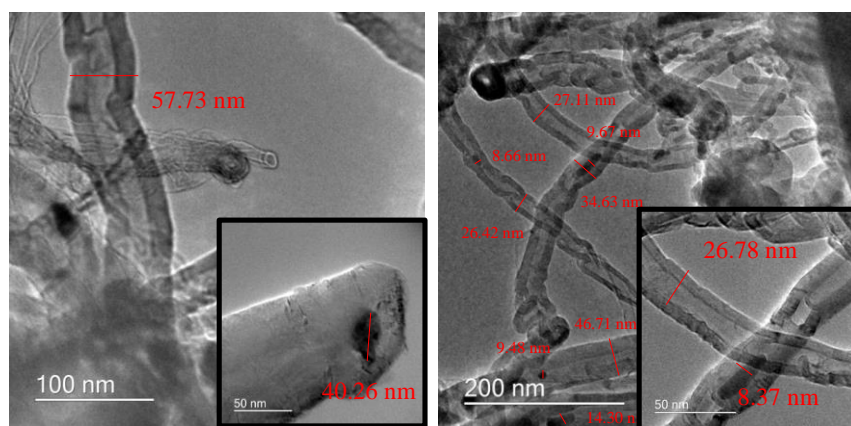

331
(b)1Mn10Fe

332
333
(c) 5Mn10Fe

334

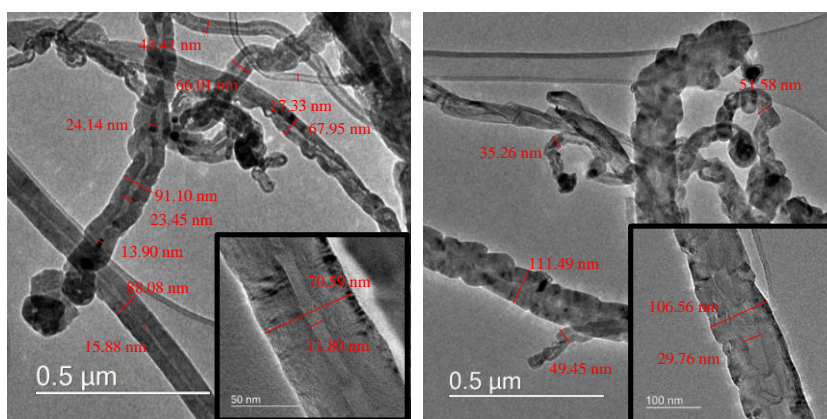335   (d) 10Mn10Fe

336   **Fig. 7.** SEM morphology analysis of the fresh (left) and reacted (right) Mn containing Fe-based

337   catalysts: (a) 0Mn10Fe (b) 1Mn10Fe, (c) 5Mn10Fe and (d) 10Mn10Fe.

338

339   (a) 0Mn10Fe   (b) 1Mn10Fe

340   (c) 5Mn10Fe   (d) 10Mn10Fe

341 **Fig. 8.** TEM of the carbon deposition on the reacted Mn containing Fe-based catalysts: (a)
342 0Mn10Fe (b) 1Mn10Fe, (c) 5Mn10Fe and (d) 10Mn10Fe.

343 **3.2.4 Raman spectra of the reacted catalysts**

344   Raman spectroscopy analysis was performed to characterise the structure of amorphous
345 and/or graphitic carbon and estimate the purity of CNTs (DiLeo et al., 2007; Ferrari and
346 Robertson, 2004). As shown in Fig.9, the Raman spectrum at wavelength of 1000-3000 cm^{-1}
347 are presented to compare the carbons produced from the four Fe-based catalysts with varied
348 Mn contents from 0-10wt.%. The Raman spectra are dominated by three vibration bands
349 characteristic of the Raman vibrations of carbonaceous materials: the D band at ~1345 cm^{-1}
350 arises from amorphous carbon or disordered carbon within structural defects; the G band at
351 ~1573 cm^{-1} arises from the sp^2 stretching vibration of the graphitic structures and is
352 characteristic of graphitic samples; and the G' band at ~2680 cm^{-1} arises from the second-order
353 scattering process of two phonons, indicating the purity of carbons (Dresselhaus et al., 2005;
354 Saito et al., 2003). The I_D/I_G ratio obtained by the normalizing the intensity of the D band to the
355 G band could be used to evaluate the graphitization of carbons. As shown in Fig. 8, as the Mn
356 content increases from 0 wt.% to 10 wt.%, the carbon I_D/I_G ratio decreases from 0.60 to 0.40,
357 suggesting that a higher amount of Mn doping could lead to a higher ratio of graphitic carbons.
358 The $I_{G'}/I_G$ ratio could be used to estimate the purity of CNTs (DiLeo et al., 2007). The $I_{G'}/I_G$
359 ratios for 0Mn10Fe, 1Mn10Fe and 5Mn10Fe are in a similar range, which indicates that the
360 purity of the CNTs produced by the three catalysts is similar. The smallest $I_{G'}/I_G$ ratios for the
361 10Mn10Fe catalyst at 0.46 correspondes to the lowest purity of CNTs, which is aggreement
362 with the TPO results shown in Fig. 5(b). Therefore, when the addition of Mn in the catalyst is
363 below 10 wt.%, the graphitization of the produced carbon could be improved. However when
364 excessive Mn (10 wt.%) is added into the iron-based catalyst, the purity of the produced carbon
365 could be reduced.
366   Table 1 shows the comparison of our work with other different Fe-based catalyst in literatures.
367 The detailed carbon yield, as well as the morphology and quality of produced CNTs are
368 presented. It is indicated that 10Mn10Fe produces a high yield of carbons in comparing with
369 other works. In addition, a large portion of the generated gases were trapped in condensation
370 system before passing through the second stage of reactor, which decreases the carbon
371 feedstock for CNTs growth, thus, could decrease the 10Mn10Fe catalyst capacity to produce
372 the highest carbon yield. The excellent catalytic performance could be partially attributed to
373 the addition of Mn. In addition, the CNTs grow on 10Mn10Fe catalyst have the lowest I_D/I_G
374 ratio value, indicating that the produced CNTs are better graphitized than other catalysts. This
375 could be also partially attributed to the promoting graphitization of Mn in the Fe-based catalysts.
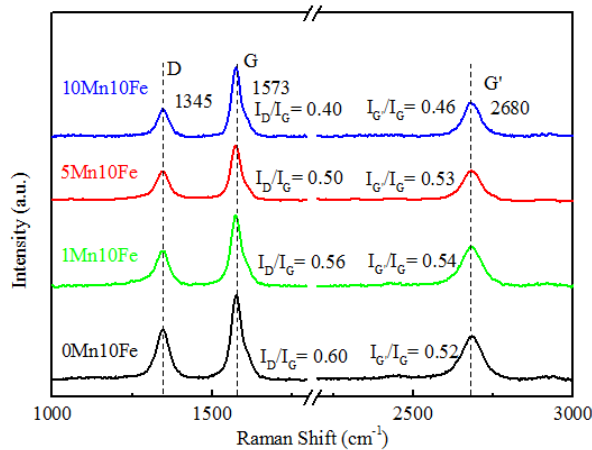
376

Fig. 9. Raman spectra of reacted catalysts.

Table 1

Comparison of carbon yield and Raman results between our research results and reports in literatures.

Feedstock	Catalyst	Carbon yield (wt.%) [a]	I_D/I_G	Ref.
PP	10Mn10Fe	41.5	0.4	This work
LDPE	Fe/Al_2O_3	34.2	0.51	(Acomb et al., 2016)
Waste tires	Fe/Al_2O_3	21.9	0.89	(Zhang et al., 2015)
PP	Fe/Cordierte	3	-	(Wang et al., 2019)
Realworld plastics	$Fe/\square\text{-}Al_2O_3$	41.3	0.64	(Yao et al., 2018b)
	$Fe/\square\text{-}Al_2O_3$	39.5	0.62	
PP	$Fe/SiO_2\text{-}S$	39.4	-	(Wu et al., 2017a)
	$Fe/SiO_2\text{-}L$	42.0	-	

[a] Obtained from the recalculation of carbon yield reported from temperature programme oxidation analysis.

Conclusion

In this study, the addition of Mn into Fe-based catalysts with content at 0 wt.%, 1wt.%, 5 wt.% and 10 wt.% have been investigated for catalytic pyrolysis of PP into CNTs. Mn is an effective promoter in the Fe-based catalyst for CNTs growth from catalytic pyrolysis of PP. The enhanced metal-support interactions by Mn addition leads to a higher yield of carbons. The dispersion of iron nanoparticles is also enhanced by Mn, inhibiting the sintering of iron particles.

In addition, the iron oxide phase is stabilized by Mn addition, therefore contributing to the stability of catalytic Fe sites. Meanwhile, the catalyst with higher Mn content favours the formation of carbides at lower carbon concentration which promotes graphite precipitation from carbides intermediates. Owing to these effects, the yield and graphitization degree of the produced CNTs increases as Mn loading increases. However, the increased Mn loading in Fe-based catalyst has negative influence on the purity of produced CNTs. Although the 10Mn10Fe catalyst produces the highest carbon yield (41.58 wt.%) than other catalysts, the mass ratio of CNTs is much lower than the 5Mn10Fe catalyst.

Acknowledgment

References

Acomb, J.C., Wu, C., Williams, P.T., 2016. The use of different metal catalysts for the simultaneous production of carbon nanotubes and hydrogen from pyrolysis of plastic feedstocks. Appl. Catal. B Environ. 180, 497–510. https://doi.org/10.1016/j.apcatb.2015.06.054

Amelinckx, S., Zhang, X.B., Bernaerts, D., Zhang, X.F., Ivanov, V., Nagy, J.B., 1994. A Formation Mechanism for Catalytically Grown Helix-Shaped Graphite Nanotubes. Science (80-.). 265, 635–639. https://doi.org/10.1126/science.265.5172.635

Andrews, R., Jacques, D., Qian, D., Rantell, T., 2002. Multiwall carbon nanotubes: Synthesis and application. Acc. Chem. Res. 35, 1008–17. https://doi.org/10.1021/ar010151m

Becker, M.J., Xia, W., Tessonnier, J.P., Blume, R., Yao, L., Schlögl, R., Muhler, M., 2011. Optimizing the synthesis of cobalt-based catalysts for the selective growth of multiwalled carbon nanotubes under industrially relevant conditions. Carbon N. Y. 49, 5253–5264. https://doi.org/10.1016/j.carbon.2011.07.043

Bezemer, G.L., Radstake, P.B., Falke, U., Oosterbeek, H., Kuipers, H.P.C.E., Van Dillen, A.J., De Jong, K.P., 2006. Investigation of promoter effects of manganese oxide on carbon nanofiber-supported cobalt catalysts for Fischer-Tropsch synthesis. J. Catal. 237, 152–161. https://doi.org/10.1016/j.jcat.2005.10.031

Bianco, A., Kostarelos, K., Prato, M., 2005. Applications of carbon nanotubes in drug delivery. Curr. Opin. Chem. Biol. 9, 674–679. https://doi.org/10.1016/j.cbpa.2005.10.005

Cheung, C.L., Kurtz, A., Park, H., Lieber, C.M., 2002. Diameter-controlled synthesis of carbon nanotubes. J. Phys. Chem. B 106, 2429–2433. https://doi.org/10.1021/jp0142278

Deck, C.P., Vecchio, K., 2006. Prediction of carbon nanotube growth success by the analysis

425   of carbon-catalyst binary phase diagrams. Carbon N. Y. 44, 267–275.
426   https://doi.org/10.1016/j.carbon.2005.07.023

427   DiLeo, R.A., Landi, B.J., Raffaelle, R.P., 2007. Purity assessment of multiwalled carbon
428   nanotubes by Raman spectroscopy. J. Appl. Phys. 101. https://doi.org/10.1063/1.2712152

429   Ding, F., Rosén, A., Bolton, K., 2004. Molecular dynamics study of the catalyst particle size
430   dependence on carbon nanotube growth. J. Chem. Phys. 121, 2775–2779.
431   https://doi.org/10.1063/1.1770424

432   Ding, M., Qiu, M., Liu, J., Li, Y., Wang, T., Ma, L., Wu, C., 2013. Influence of manganese
433   promoter on co-precipitated Fe-Cu based catalysts for higher alcohols synthesis. Fuel 109, 21–
434   27. https://doi.org/10.1016/j.fuel.2012.06.034

435   Dresselhaus, M.S., Dresselhaus, G., Saito, R., Jorio, A., 2005. Raman spectroscopy of carbon
436   nanotubes. Phys. Rep. 409, 47–99. https://doi.org/10.1016/j.physrep.2004.10.006

437   Drzyzga, O., Prieto, A., 2019. Plastic waste management, a matter for the 'community.' Microb.
438   Biotechnol. 12, 66–68. https://doi.org/10.1111/1751-7915.13328

439   Ferrari, A.C., Robertson, J., 2004. Raman spectroscopy of amorphous, nanostructured,
440   diamond-like carbon, and nanodiamond. Philos. Trans. R. Soc. A Math. Phys. Eng. Sci. 362,
441   2477–2512. https://doi.org/10.1098/rsta.2004.1452

442   Feyzi, M., Jafari, F., 2012. Study on iron-manganese catalysts for Fischer-Tropsch synthesis.
443   Ranliao Huaxue Xuebao/Journal Fuel Chem. Technol. 40, 550–557.
444   https://doi.org/10.1016/s1872-5813(12)60021-8

445   Hayashi, T., Kohno, H., 2020. Diameter-Modulated Multi-Walled Carbon Nanotubes Without
446   Bamboo-Like Partitions: Growth, Structure and Deformation Behaviors. J. Nanosci.
447   Nanotechnol. 20, 3038–3041. https://doi.org/https://doi.org/10.1166/jnn.2020.17451

448   He, M., Fedotov, P. V., Chernov, A., Obraztsova, E.D., Jiang, H., Wei, N., Cui, H., Sainio, J.,
449   Zhang, W., Jin, H., Karppinen, M., Kauppinen, E.I., Loiseau, A., 2016. Chiral-selective growth
450   of single-walled carbon nanotubes on Fe-based catalysts using CO as carbon source. Carbon N.
451   Y. 108, 521–528. https://doi.org/10.1016/j.carbon.2016.07.048

452   Iijima, S., 1991. Helical microtubules of graphitic carbon. Nature 354, 56–58.
453   https://doi.org/https://doi.org/10.1038/354056a0

454   Jia, J., Zhang, P., Chen, L., 2016. The effect of morphology of α-MnO2 on catalytic
455   decomposition of gaseous ozone. Catal. Sci. Technol. 6, 5841–5847.
456   https://doi.org/10.1039/c6cy00301j

457   Karásková, K., Obalová, L., Jirátová, K., Kovanda, F., 2010. Effect of promoters in Co-Mn-Al
458   mixed oxide catalyst on N2O decomposition. Chem. Eng. J. 160, 480–487.
459   https://doi.org/10.1016/j.cej.2010.03.058

460 Kotov, V., Sviatenko, A., Nebesnyi, A., Filonenko, D., Khovavko, A., Bondarenko, B., 2019.
461 CNTs growth on reduced iron. Mater. Today Proc. https://doi.org/10.1016/j.matpr.2019.11.287

462 Landi, B.J., Ganter, M.J., Cress, C.D., DiLeo, R.A., Raffaelle, R.P., 2009. Carbon nanotubes
463 for lithium ion batteries. Energy Environ. Sci. 2, 638–654. https://doi.org/10.1039/b904116h

464 Lebreton, L., Andrady, A., 2019. Future scenarios of global plastic waste generation and
465 disposal. Palgrave Commun. 5, 1–11. https://doi.org/10.1057/s41599-018-0212-7

466 Lee, M.D., Lee, J.F., Chang, C.S., Dong, T.Y., 1991. Effects of addition of chromium,
467 manganese, or molybdenum to iron catalysts for carbon dioxide hydrogenation. Appl. Catal.
468 72, 267–281. https://doi.org/10.1016/0166-9834(91)85055-Z

469 Leith, I.R., Howden, M.G., 1988. Temperature-programmed reduction of mixed iron-
470 manganese oxide catalysts in hydrogen and carbon monoxide. Appl. Catal. 37, 75–92.
471 https://doi.org/10.1016/S0166-9834(00)80752-6

472 Lettieri, P., Al-Salem, S.M., 2011. Thermochemical Treatment of Plastic Solid Waste, Waste.
473 Elsevier Inc. https://doi.org/10.1016/B978-0-12-381475-3.10017-8

474 Lin, J., Yang, Yihang, Zhang, H., Li, F., Yang, Yulin, 2020. Carbon nanotube growth on
475 titanium boride powder by chemical vapor deposition: Influence of nickel catalyst and carbon
476 precursor supply. Ceram. Int. 46, 12409–12415.
477 https://doi.org/10.1016/j.ceramint.2020.02.002

478 Liu, Y., Qian, W., Zhang, Q., Ning, G., Luo, G., Wang, Y., Wang, D., Wei, F., 2009. Synthesis
479 of high-quality, double-walled carbon nanotubes in a fluidized bed reactor. Chem. Eng.
480 Technol. 32, 73–79. https://doi.org/10.1002/ceat.200800298

481 Modekwe, H.U., Mamo, M., Moothi, K., Daramola, M.O., 2020. Synthesis of bimetallic
482 NiMo/MgO catalyst for catalytic conversion of waste plastics (polypropylene) to carbon
483 nanotubes (CNTs) via chemical vapour deposition method. Mater. Today Proc.
484 https://doi.org/10.1016/j.matpr.2020.02.398

485 Nahil, M.A., Wu, C., Williams, P.T., 2015. Influence of metal addition to Ni-based catalysts
486 for the co-production of carbon nanotubes and hydrogen from the thermal processing of waste
487 polypropylene. Fuel Process. Technol. 130, 46–53.
488 https://doi.org/10.1016/j.fuproc.2014.09.022

489 Nasser, A.H., Guo, L., Elnaggar, H., Wang, Y., Guo, X., Abdelmoneim, A., Tsubaki, N., 2018.
490 Mn-Fe nanoparticles on a reduced graphene oxide catalyst for enhanced olefin production from
491 syngas in a slurry reactor. RSC Adv. 8, 14854–14863. https://doi.org/10.1039/c8ra02193g

492 Nerushev, O.A., Dittmar, S., Morjan, R.-E., Rohmund, F., Campbell, E.E.B., 2003. Particle
493 size dependence and model for iron-catalyzed growth of carbon nanotubes by thermal chemical
494 vapor deposition. J. Appl. Phys. 93, 4185–4190. https://doi.org/10.1063/1.1559433

495 Pineau, A., Kanari, N., Gaballah, I., 2006. Kinetics of reduction of iron oxides by H2. Part I:
496 Low temperature reduction of hematite. Thermochim. Acta 447, 89–100.
497 https://doi.org/10.1016/j.tca.2005.10.004

498 Ran, M., Chu, W., Liu, Y., Liu, D., Zhang, C., Zheng, J., 2014. Doping effects of manganese
499 on the catalytic performance and structure of NiMgO catalysts for controllabe synthesis of
500 multi-walled carbon nanotubes. J. Energy Chem. 23, 781–788. https://doi.org/10.1016/S2095-
501 4956(14)60212-6

502 Saito, R., Grüneis, A., Samsonidze, G.G., Brar, V.W., Dresselhaus, G., Dresselhaus, M.S., Jorio,
503 A., Cançado, L.G., Fantini, C., Pimenta, M.A., Souza Filho, A.G., 2003. Double resonance
504 Raman spectroscopy of single-wall carbon nanotubes. New J. Phys. 5.
505 https://doi.org/10.1088/1367-2630/5/1/157

506 Shah, K.A., Tali, B.A., 2016. Synthesis of carbon nanotubes by catalytic chemical vapour
507 deposition: A review on carbon sources, catalysts and substrates. Mater. Sci. Semicond. Process.
508 41, 67–82. https://doi.org/10.1016/j.mssp.2015.08.013

509 Sivakumar, V.M., Abdullah, A.Z., Mohamed, A.R., Chai, S.P., 2011. Optimized parameters for
510 carbon nanotubes synthesis over Fe and Ni catalysts VIA methane CVD. Rev. Adv. Mater. Sci.
511 27, 25–30.

512 Tang, W., Wu, X., Li, D., Wang, Z., Liu, G., Liu, H., Chen, Y., 2014. Oxalate route for
513 promoting activity of manganese oxide catalysts in total VOCs' oxidation: Effect of calcination
514 temperature and preparation method. J. Mater. Chem. A 2, 2544–2554.
515 https://doi.org/10.1039/c3ta13847j

516 Wang, J., Shen, B., Lan, M., Kang, D., Wu, C., 2019. Carbon nanotubes (CNTs) production
517 from catalytic pyrolysis of waste plastics: The influence of catalyst and reaction pressure. Catal.
518 Today 1–8. https://doi.org/10.1016/j.cattod.2019.01.058

519 Wu, C., Liu, X., Williams, P.T., Nahil, M.A., Zhang, Y., 2017a. Development of Ni- and Fe-
520 based catalysts with different metal particle sizes for the production of carbon nanotubes and
521 hydrogen from thermo-chemical conversion of waste plastics. J. Anal. Appl. Pyrolysis 125, 32–
522 39. https://doi.org/10.1016/j.jaap.2017.05.001

523 Wu, C., Nahil, M.A., Miskolczi, N., Huang, J., Williams, P.T., Engineering, P., Ls, L., 2017b.
524 Production and application of carbon nanotubes , as a co-product of hydrogen from the
525 pyrolysis-catalytic reforming of waste plastic. Process Saf. Environ. Prot. 103, 107–114.
526 https://doi.org/10.1016/j.psep.2016.07.001

527 Wu, C., Williams, P.T., 2009. Hydrogen production from the pyrolysis-gasification of
528 polypropylene: Influence of steam flow rate, carrier gas flow rate and gasification temperature.
529 Energy and Fuels 23, 5055–5061. https://doi.org/10.1021/ef900278w

530 Xu, J.D., Zhu, K.T., Weng, X.F., Weng, W.Z., Huang, C.J., Wan, H.L., 2013a. Carbon
531 nanotube-supported Fe-Mn nanoparticles: A model catalyst for direct conversion of syngas to

532   lower olefins. Catal. Today 215, 86–94. https://doi.org/10.1016/j.cattod.2013.04.018

533   Xu, J.D., Zhu, K.T., Weng, X.F., Weng, W.Z., Huang, C.J., Wan, H.L., 2013b. Carbon
534   nanotube-supported Fe-Mn nanoparticles: A model catalyst for direct conversion of syngas to
535   lower olefins. Catal. Today 215, 86–94. https://doi.org/10.1016/j.cattod.2013.04.018

536   Yan, Y., Miao, J., Yang, Z., Xiao, F.X., Yang, H. Bin, Liu, B., Yang, Y., 2015. Carbon nanotube
537   catalysts: Recent advances in synthesis, characterization and applications. Chem. Soc. Rev. 44,
538   3295–3346. https://doi.org/10.1039/c4cs00492b

539   Yang, R.X., Chuang, K.H., Wey, M.Y., 2015. Effects of Nickel Species on Ni/Al2O3 Catalysts
540   in Carbon Nanotube and Hydrogen Production by Waste Plastic Gasification: Bench- and Pilot-
541   Scale Tests. Energy and Fuels 29, 8178–8187. https://doi.org/10.1021/acs.energyfuels.5b01866

542   Yang, Y., Xiang, H.W., Tian, L., Wang, H., Zhang, C.H., Tao, Z.C., Xu, Y.Y., Zhong, B., Li,
543   Y.W., 2005. Structure and Fischer-Tropsch performance of iron-manganese catalyst
544   incorporated with   SiO2.   Appl.   Catal.   A   Gen.   284,   105–122.
545   https://doi.org/10.1016/j.apcata.2005.01.025

546   Yang, Y., Xiang, H.W., Xu, Y.Y., Bai, L., Li, Y.W., 2004. Effect of potassium promoter on
547   precipitated iron-manganese catalyst for Fischer-Tropsch synthesis. Appl. Catal. A Gen. 266,
548   181–194. https://doi.org/10.1016/j.apcata.2004.02.018

549   Yao, D., Zhang, Y., Williams, P.T., Yang, H., Chen, H., 2018. Co-production of hydrogen and
550   carbon nanotubes from real-world waste plastics: Influence of catalyst composition and
551   operational   parameters.   Appl.   Catal.   B   Environ.   221,   584–597.
552   https://doi.org/10.1016/j.apcatb.2017.09.035

553   Zein, S.H.S., Mohamed, A.R., 2004. Mn/Ni/TiO2 catalyst for the production of hydrogen and
554   carbon nanotubes from methane decomposition. Energy and Fuels 18, 1336–1345.
555   https://doi.org/10.1021/ef0340864

556   Zghal, S., Jedidi, I., Cretin, M., Cerneaux, S., Abdelmouleh, M., 2020. One-step synthesis of
557   highly porous carbon graphite/carbon nanotubes composite by in-situ growth of carbon
558   nanotubes for the removal of humic acid and copper (II) from wastewater. Diam. Relat. Mater.
559   101, 107557. https://doi.org/10.1016/j.diamond.2019.107557

560   Zhang, T., Wang, Q., Lv, X., Luo, Y., Zhang, Y., 2020. Transformation of primary siderite
561   during coal catalytic pyrolysis and its effects on the growth of carbon nanotubes. Fuel Process.
562   Technol. 198, 106235. https://doi.org/10.1016/j.fuproc.2019.106235

563   Zhang, Y., Nahil, M.A., Wu, C., Williams, P.T., 2017. Pyrolysis–catalysis of waste plastic
564   using a nickel–stainless-steel mesh catalyst for high-value carbon products. Environ. Technol.
565   (United Kingdom) 38, 2889–2897. https://doi.org/10.1080/09593330.2017.1281351

566   Zhang, Y., Wu, C., Nahil, M.A., Williams, P., 2015. Pyrolysis-catalytic reforming/gasification
567   of waste tires for production of carbon nanotubes and hydrogen. Energy and Fuels 29, 3328–

568   3334. https://doi.org/10.1021/acs.energyfuels.5b00408

569   Zhao, A., Ying, W., Zhang, H., Hongfang, M., Fang, D., 2012. Ni/Al 2O 3 catalysts for syngas
570   methanation: Effect of Mn promoter. J. Nat. Gas Chem. 21, 170–177.
571   https://doi.org/10.1016/S1003-9953(11)60350-2

572

1 **Waste plastics recycling for producing high-value carbon nanotubes: Investigation of**
2 **the influence of Manganese content in Fe-based catalysts**

3 Su He[a], Yikai Xu[a], Yeshui Zhang[b], Steven Bell[a], Chunfei Wu[a]*

4 *[a] School of Chemistry and Chemical Engineering, Queen's University Belfast, Belfast, BT7*

5 *1NN, UK*

6 *[b] Electrochemical Innovation Lab (EIL), Department of Chemical Engineering, University*

7 *College London, London, WC1E 7JE, UK*

8 ** Corresponding authors: E-mail: c.wu@qub.ac.uk (C. Wu)*

9 **Abstract**

10 Thermo-chemical conversion is a promising technology for the recycle of waste plastics, as it
11 can produce high-value products such as carbon nanotubes (CNTs) and hydrogen. However,
12 the low yield of CNTs is one of the challenges. In this work, the addition of Mn (0 wt.%, 1
13 wt.%, 5 wt.%, and 10 wt.%) to Fe-based catalyst to improve the production of CNTs has been
14 investigated. Results show that the increase of Mn content from 0 wt.% to 10 wt.% significantly
15 promotes CNTs yield formed on the catalyst from 23.4 wt.% to 32.9 wt.%. The results show
16 that Fe-particles in the fresh catalysts are between 10-25 nm. And the addition of Mn in the Fe-
17 based catalyst enhanced the metal-support interactions and the dispersion of metal particles,
18 thus leading to the improved catalytic performance in relation to filamentous carbon growth. In
19 addition, the graphitization of CNTs is promoted with the increase of Mn content. Overall, in
20 terms of the quantity and quality of the produced CNTs, 5 wt.% of Mn in Fe-based catalyst
21 shows the best catalytic performance, due to the further increase of Mn content from 5 wt.% to
22 10 wt.% led to a dramatic decrease of purity by 10 wt.%.
23
24 Keywords: Waste plastics; carbon nanotubes; Mn-catalyst; thermo-chemical processing;
25 pyrolysis
26

1. Introduction

Nowadays, plastics are used in various aspects, from household goods such as packaging, clothing, electrical devices, to industrial applications such as automotive parts and insulations (Lettieri and Al-Salem, 2011). The vast demand for plastic results in increasing plastic production year by year. In 2016, plastic production reached 330 million tons and will double within the next 20 years under the current estimationed growth rate (Lebreton and Andrady, 2019). The extensive use of plastics generates a large amunt of wastes. These waste plastics cause severe environmental pollution if they were not well managed. The general methods for plastics waste management include landfill, energy recovery and recycling. Landfill is the most common method for plastic waste treatment in developing countries due to the cheap cost. Even in Europe, ~31 % of waste plastics still goes to land fill, wasting energy stored in the plastic and also causing severe environmental challenges (Drzyzga and Prieto, 2019; Lebreton and Andrady, 2019). In pricinple, recycling of plastic waste provides a more economical and environmental-friendly solution. However, current state of the art technologies of plastic wastes recycling mostly produce low-value products, such as cricks and road construction materials. Therefore, converting waste plastics into high-value products such as carbon nanotubes (CNTs) is a promising alternative for plastic waste management.

Since its discovery by Iijima in 1991 (Iijima, 1991), the extraordinary mechanical and electrical properties of CNTs have allowed it to find a variety of potential applications, such as drug delivery (Bianco et al., 2005), energy storage (Landi et al., 2009), materials strengthening (Andrews et al., 2002), etc. As a result, CNTs production from catalytic pyrolysis of plastic waste has been obtaining increasing interest. The key component to plastic pyrolysis is the catalyst which determins both the yield and quality of the produced CNTs.

In the chemical vapour deposition (CVD) synthesis of CNTs from various carbon feedstocks, Fe, Co and Ni are the most effective and widely used catalysts (Shah and Tali, 2016). The using of different catalysts could lead to the different properties and yield of CNTs. Lee et al. investigated the influence of Fe, Co and Ni-silica supported catalysts and reported that Fe catalyst resulted in the best crystallinity of produced CNTs. Sivakumar et al. reported that the produced CNTs over Ni catalyst have higher thermal stability than Fe catalyst (Sivakumar et al., 2011). In addition, the morphology and quality of the produced CNTs were also strongly affected by carbon feedstocks (Yan et al., 2015). In the catalytic synthesis of CNTs using plastic as carbon source, extensive researches have also been conducted on a range of metals e.g. Fe (Wu et al., 2017a), Ni (Yao et al., 2018) and Co (Acomb et al., 2016). Acomb et al. produced CNTs using Fe/Al_2O_3 catalyst from catalytic pyrolysis of LDPE (Low-Density Polyethylene) and obtained carbon deposition yielded 26 wt.% (Acomb et al., 2016). Yao et al. reported using $Fe/\alpha-Al_2O_3$ and $Fe/\gamma-Al_2O_3$ catalyst to produce CNTs from real world plastics, and the carbon yielded 35.2 and 32.6 wt.%, respectively (Yao et al., 2018). In Wu et al's work, Fe/SiO_2 catalysts were used to produce CNTs with carbon yield 29 wt.% from PP(Wu et al., 2017a). In the previous work, compared to Ni or Co based catalyst, Fe-based catalysts lead to a higher yield of carbon from catalytic conversion of plastics, which is owing to the higher carbon solubility and higher carbon diffusion rate of iron nanoparticles (Deck and Vecchio, 2006) as well as the appropriate strength of metal-support interactions (Acomb et al., 2016).

Mn acting as an effective promoter was used in a variety catalytic reactions, such as the

70   Fischer–Tropsch process (Bezemer et al., 2006; Ding et al., 2013; Xu et al., 2013a; Zhao et al.,
71   2012), volatile organic compounds oxidation (Tang et al., 2014), and the decomposition of
72   nitrous oxides (Jia et al., 2016; Karásková et al., 2010). As for the synthesis of CNTs, Mn as a
73   promoter in Ni-based and Co-based catalysts have also been reported from various carbon
74   feedstocks (Zein and Mohamed, 2004)(Nahil et al., 2015)(Wu et al., 2017b). The promoting
75   effects of Mn in Ni-based catalyst for CNTs synthesis from methane were reported by several
76   researchers. For example, Zein et. al reported Mn-Ni/TiO$_2$ catalysts prepared by three different
77   methods for the production of hydrogen and CNTs from methane (Zein and Mohamed, 2004).
78   However, only a fixed content of Mn (15 wt.%) was used in the research, and the reasons for
79   the catalytic performance was not clear. Ran et. al further investigated the doping effect of Mn
80   on CNTs formation in the presence of Ni/MgO catalysts with varied Mn content. It was found
81   that the addition of Mn to the Ni/MgO catalyst significantly increased the carbon yield, with
82   the highest carbon yield produced by the catalyst with Mn:Ni a molar ratio of 0.2:1 (Ran et al.,
83   2014). In addition, Becker et al. reported that Mn-Co catalysts with Mn:Co molar ratio of 1:1
84   led to the highest CNTs yield using ethene as carbon source (Becker et al., 2011). He et. al
85   applied Mn-Fe/MgO catalyst to improve the chirality distribution of the produced single-walled
86   CNTs using CO as carbon source (He et al., 2016).

87   Mn's promoting effects have also been investigated in the CNTs synthesis from waste
88   plastics. In Nahil et. al's work, a variety of metals (Zn, Mg, Ca, Ce, Mo, Mn, etc.) added into
89   Ni-based catalysts have been investigated for the catalytic conversion of waste plastics
90   (polypropylene) into CNTs (Nahil et al., 2015). It was found that the addition of Mn into Ni-
91   based catalyst resulted in the highest yield of CNTs. Further work by Wu et al. investigated the
92   effects of Mn content on CNTs synthesis in the Ni-based catalyst. The Mn-Ni/Al$_2$O$_3$ catalyst
93   with Mn:Ni a molar ratio of 2:2 produced a higher yield of carbon compared to Mn:Ni with a
94   molar ratio of 2:1 in the synthesis of CNTs using waste plastics (polypropylene) as carbon
95   feedstock.

96   Owing to the great catalytic performance of Fe-based catalyst and Mn as a promising
97   promoter in CNTs formation from plastics, there is a potential of further increasing CNTs
98   production and quality by doping Mn into Fe-based catalyst during catalytic conversion of
99   waste plastics. Therefore, in this work, we report the influence of Mn content in the Fe-based
100   catalyst for CNTs production from catalytic pyrolysis of waste plastics. This work aims to
101   optimise the development of Fe-based catalysts by adding Mn in relation to CNTs production
102   from waste plastics.

103   **2. Experimental**

104   **2.1 Materials and preparation of catalyst**

105   The plastic raw material used in this study was recycled polypropylene (PP) pellet
106   obtained from regain polymer Ltd. with a diameter of ~2mm. The chemicals
107   Mn(NO$_3$)$_2$•H$_2$O (98%, Sigma-Aldrich, cat. no. 288640) and Fe(NO$_3$)$_3$•9H$_2$O (≥98%,
108   ACS reagent, Sigma-Aldrich, cat. no. 16828) were used as starting materials. Al$_2$O$_3$
109   (≥98%, puriss, Sigma-Aldrich, cat. no. 11028) with particle size around 10 μm is used
110   as the catalyst support. All materials were used directly without any pre-treatment.
111   MnFe/Al$_2$O$_3$ catalysts were prepared by a wet impregnation method. The catalysts

112 contain 10 wt.% of Fe. The content of Mn is 0 wt.%, 1 wt.%, 5 wt.% and 10 wt.%,
113 respectively. And the corresponding catalyst is assigned as 0Mn10Fe, 1Mn10Fe,
114 5Mn10Fe and 10Mn10Fe, respectively. For comparison, a catalyst with 10 wt.% Mn
115 without Fe (10Mn0Fe) was prepared use the same method.

116 During catalyst preparation, the required amount of $Mn(NO_3)_2 \cdot xH_2O$ and $Fe(NO_3)_3 \cdot 9H_2O$
117 were dissolved in 100 ml of deionized water, and the mixture solution was stirred for ~0.5 h
118 until the chemicals were fully dissolved. The required amount of Al_2O_3 was then slowly added
119 into the mixture solution and stirred for ~1 h. After that, water was removed by evaporation at
120 90 °C, followed by drying in an oven at 105 °C overnight to remove the remaining water.
121 Finally, the dried catalyst precursors were grounded into a fine powder and then were heated
122 in the air atmosphere at a heating rate of 10 °C min^{-1} to 500 °C for 3 h of calcination.

2.2 Catalytic pyrolysis of plastic waste into CNTs

124 The catalytic pyrolysis of plastic waste into CNTs was performed in a two-stage reactor in
125 this study. Fig. 1 shows the schematic diagram of this reaction system. The first-stage reactor
126 consists of a horizontal quartz tube placed in a tubular furnace for PP pyrolysis. The generated
127 vapor was carried by N_2 with a flow rate of 100 ml min^{-1} and after condensation, the non-
128 condensed products passed through the second-stage of the reactor.

129 For each run of the experiment, 2 g of PP was located inside an aluminium boat in the centre
130 of the first-stage reactor, and 0.5 g of catalyst supported by ~30 mg of quartz wool was located
131 in the centre of the second-stage reactor. The reaction system was purged by N_2 for ~10 min
132 before the second-stage reactor started to heat from room temperature to 800 °C with a heating
133 rate of 40 °C min^{-1}. When the second-stage reactor reached the set point temperature, the first-
134 stage reactor containing 2 g of PP started to heat from room temperature to 200 °C with a
135 heating rate of 40 °C min^{-1}, followed by heating from 200 °C to 500 °C with a heating rate of
136 10 °C min^{-1}. After ~1 h of reaction time, the reaction system was slowly cooled down to room
137 temperature under N_2 protection, and the reacted catalyst together with the produced CNTs
138 were collected for further characterisations. The Fe-based catalysts with different Mn contents
139 associated with the production of CNTs were studied.
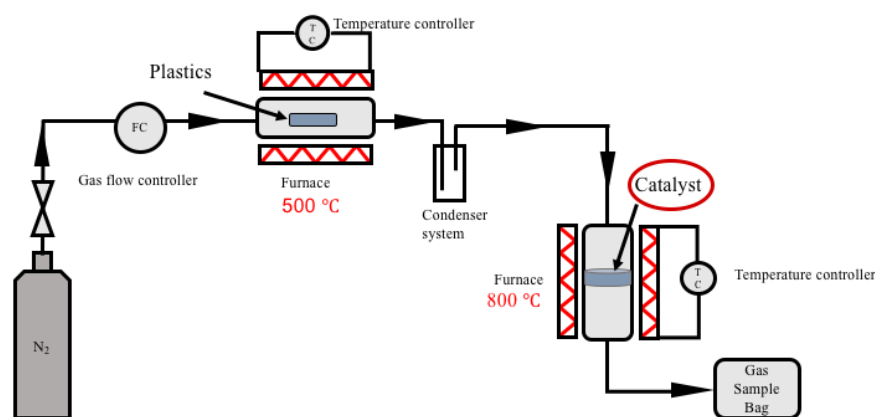
140
141 **Fig. 1.** Schematic diagram of the two-stage reaction system.

2.3 Characterisation of fresh and reacted catalyst

143   TA Instruments TGA 2950 thermogravimetric analyser (TGA) was used to analyse the
144   temperature programme reduction (TPR) of the fresh catalyst to observe the reduction of the
145   catalyst metal. Under a mixed gas of H_2 and N_2 gas (5 vol.% : 95 vol.%), ~50 mg of catalyst
146   was heated from room temperature to 100 °C at a heating rate of 10 °C min^{-1} and held for 10
147   min, then the temperature increased to 950 °C under at the same heating rate to record the TPR
148   curve.
149   Temperature programme oxidation (TPO) analysis for the reacted catalysts was conducted
150   by the same TGA 2950 equipment using air gas to measure the amount of carbon formed on
151   the reacted catalyst and to distinguish different types of carbons, such as amorphous carbons or
152   graphite. For each TPO process, ~30 mg of reacted catalyst sample was heated to 800 °C in air
153   at a heating rate of 15 °C min^{-1}. The fresh and reacted catalysts were also characterized by a
154   Panalytical X-ray diffraction (XRD) equipment with a scanning step of 0.033º using
155   Cu•kα1 radiation in the range from 5º to 80º and the data was analysed with Highscore software.
156   The strongest peak was chosen to calculate the crystallite size by Scherrer equation. The surface
157   morphology and diameter of the metal particles of the catalysts were observed with a FEI
158   Quanta FEG Oxford Ex-ACT scanning electron microscope (SEM) and a Jeol 2100 LaB6
159   transmission electron microscope (TEM). The WITec Alpha 300R Confocal Raman
160   Microscope equipped with a 532 nm diode laser with an output power of 30 mWwas used to
161   perform Raman spectroscopic analysis of the reacted catalyst.

3. Results and discussion

3.1 Characterization of fresh catalysts

164   XRD results of the prepared Fe-based catalysts with varied Mn contents are shown in Fig. 2.
165   In general, the diffraction patterns of all four catalysts are dominated by the characteristic peaks
166   of α-Fe_2O_3 at 4.2º, 33.3º, 35.7º, 41.05º, 49.71º, 54.36º, 62.74º, 64.30º 2θ, indicating that the
167   main composition of the catalysts are α-Fe_2O_3. For the 0Mn10Fe catalyst, the diffraction
168   patterns only consist of peaks corresponding to α-Fe_2O_3 and Al_2O_3. For the Mn-doped catalysts,
169   the XRD data show weak diffraction of manganese oxides, which is in good agreement with
170   literatures (Feyzi and Jafari, 2012; Lee et al., 1991; Nasser et al., 2018; Yang et al., 2005). This
171   might be due to Mn was present as amorphous or highly dispersed on the surface of the Al_2O_3
172   support (Nasser et al., 2018).
173   The size of the α-Fe_2O_3 crystallite phase was calculated using the Scherrer equation. For the
174   0Mn10Fe catalyst, the crystallite size is 107.1 nm. Interestingly, it is found that the crystallite
175   size of 1Mn10Fe, 5Mn10Fe and 10Mn10Fe catalyst are much smaller, at 14.0 nm, 8.4 nm, and
176   30.3 nm, respectively. It is indicated that an appropriate amount of Mn dopant could
177   significantly improve the dispersion of iron in the catalyst. The crystallite size of the 10Mn10Fe
178   catalyst is larger than the 5Mn10Fe catalyst, which could be resulted from the excessive amount
179   of Mn dopant in the catalyst. It is now well-established that the size of the catalyst particles are
180   crucial for CNTs formation and that larger particles often exhibit lower catalytic activities due
181   to the reduced active-surface area (Acomb et al., 2016; Liu et al., 2009). Therefore, the above
182   findings demonstrate that an appropriate amount of Mn is required to be added to the Fe-based
183   catalyst in terms of the catalytic conversion of waste platics to form CNTs.
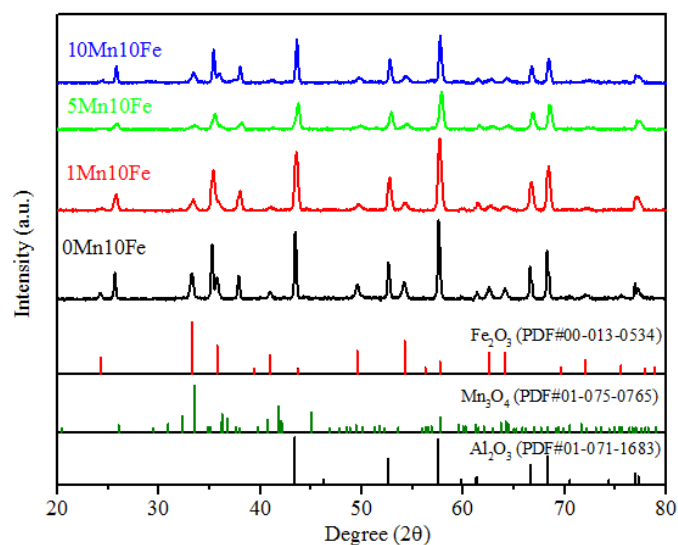
185
186 **Fig. 2**. X-ray diffraction of the freshFe-based catalysts with different amount of (Mn
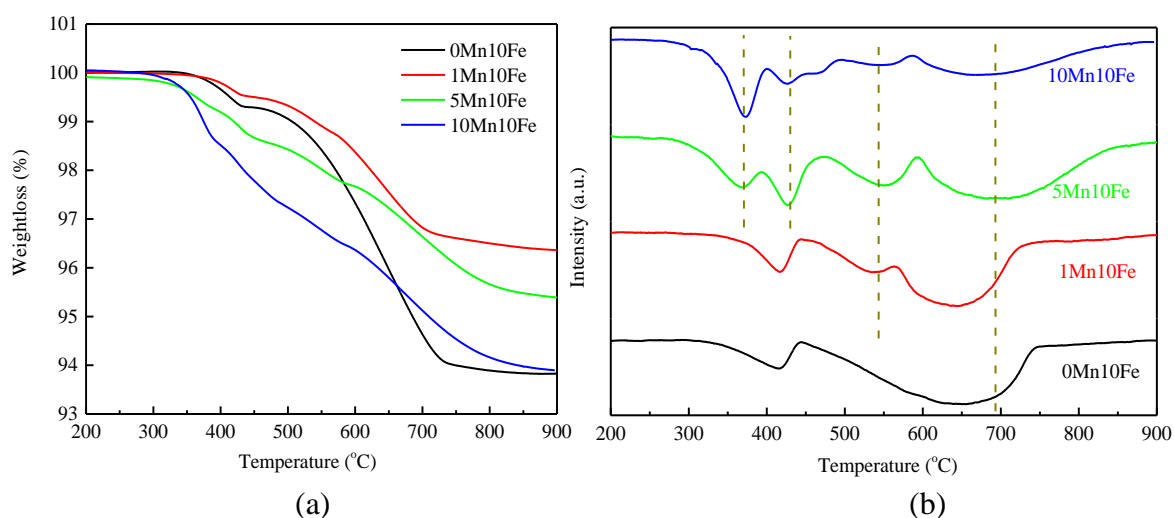187 0Mn10Fe, 1MnFe, 5Mn10Fe and 10Mn10Fe).
188

189   The H_2-TPR results for the four catalysts are shown in Fig. 3. Several reduction peaks are
190 obtained since both Fe and Mn elements possess several types of oxide forms and the reduction
191 of Fe_2O_3 and Mn_3O_4 proceed subsequentially. Hydrogen reduction of Fe_2O_3 involves two or
192 three steps according to different reduction temperatures (Pineau et al., 2006): when the
193 reduction temperature is below 570 °C, wüstite FeO was formed as an intermediate product
194 before the formation of Fe, as illustrated in Eq. (1); when the reduction temperature is above
195 570 °C, Fe_2O_3 reduced into Fe_3O_4 and then directly reduced into Fe, as shown in Eq. (2):
196     $Fe_2O_3 \rightarrow Fe_3O_4 \rightarrow FeO \rightarrow Fe$ (1)

197     $Fe_2O_3 \rightarrow Fe_3O_4 \rightarrow Fe$ (2)
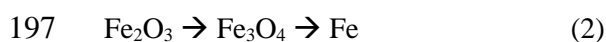
198   As indicated in Fig. 3, the 0Mn10Fe catalyst undergoes two stages of reduction. ~0.68 wt.%
199 weight loss occurred in the first stage and ~5.5 wt.% weight loss occurred in the second stage.
200 The first reduction peak at 420 °C can be attributed to the reduction of α-Fe_2O_3 to Fe_3O_4. The
201 second broad peak as illustrated in the range of 450-750 °C can be attributed to the
202 subsequentially reduction of Fe_3O_4 to FeO and Fe following Eq.(1) process. 1Mn10Fe have
203 three reduction stages, which have a weight loss of 0.47 wt.%, 0.69 wt.% and 2.47 wt.%,
204 respectively. 1Mn10Fe shows a major reduction peak in the first stage for the reduction of α-
205 Fe_2O_3 to Fe_3O_4 which shifted towards higher temperature compared to 0Mn10Fe. Meanwhile,
206 the first stage weight loss for 1Mn10Fe is lower than that compared to 0Mn10Fe. These
207 suggesting that the Mn-doped catalyst is more resistant to the reduction and the metal-support
208 interactions is enhanced with the addition of Mn. The new peak appearring at 540 °C for
209 1Mn10Fe catalyst indicates that the reduction of Fe_3O_4 to Fe via FeO is further stabilized by
210 MnO (Leith and Howden, 1988; Yang et al., 2005, 2004).The weight loss of four reduction
211 stages for the 5Mn10Fe catalyst are 0.58 wt.%, 0.61 wt.%, 0.92 wt.% and 2.4 wt.%, respectively.
212 And the 10Mn10Fe catalyst showes an obvious increase of weight loss in the first two reduction
213 peaks, which are 1.4 wt.% and 1.3 wt.%. respectively. For the third and fourth reduction stages,

214   it shows a similar weight loss value compared to the 1Mn10Fe and 5Mn10Fe catalysts. The
215   new reduction peak appears at ~370 °C for the 5Mn10Fe and 10Mn10Fe catalysts can be
216   attirbuted to the large amount of Mn_3O_4 which is reduced into Mn with MnO as intermediates.
217   This indicates the overall weight loss is increased from 3.63 wt.% to 6.1 wt.% when the Mn
218   content increases from 1 wt.% to 10 wt.% in the catalyst, but the corresponding reduction
219   weight loss for Fe_3O_4 is similar. In addition, the major α-Fe_2O_3 reduction peak for the 5Mn10Fe
220   and 10Mn10Fe catalysts shifts towards higher temperature at ~430 °C compared to the
221   1Mn10Fe catalyst, suggesting that increasing the Mn loading from 0-5 wt.% improves the
222   metal-support interactions but the further increase of Mn loading to 10 wt.% has slight impacts
223   on the metal-support interaction.
224

225   **Fig. 3.** TPR (a) and DTG-TPR (b) profiles of the fresh Fe-based catalysts with varied amount
226   of Mn in the catalysts (0Mn10Fe, 1MnFe, 5Mn10Fe and 10Mn10Fe).

227   **3.2 The production of CNTs**

228   **3.2.1 Temperature programmed oxidation (TPO) of the reacted catalysts**

229   TPO results of the reacted catalysts (0Mn10Fe, 1MnFe, 5Mn10Fe and 10Mn10Fe) are shown
230   in Fig.4. Based on previous work, the weight loss of amorphous carbons and filamentous
231   carbons can be distinguished using oxidation temperature due to their different oxidation
232   properties: the weight loss occurred before 600 °C corresponds to the oxidation of amorphous
233   carbon, while the weight loss occured after 600 °C is related to the oxidation of filamentous
234   carbon (assumed as CNTs in this study) (Wu and Williams, 2009; Yang et al., 2015; Zhang et
235   al., 2017). From Fig. 4(a), a slight increase of the catalyst weight between 350 and 500 °C is
236   observed due to the oxidation of Mn and Fe. For the reacted 10Mn0Fe catalyst, no weight loss
237   is observed, which indicates that almost no carbons are deposited on the surface of the reacted
238   catalyst. Therefore, it is demonstrated that the 10Mn0Fe catalyst without Fe is inactive for
239   carbon formation. However, the remaining four Fe-based catalysts show a significantly increase
240   of weight loss with increasing Mn content and the 10Mn10Fe catalyst gives the highest carbon
241   formation (~41.5 wt.% of the total catalyst), as shown in Fig.4(a). It is indicated that Fe is the
242   active sites and Mn promotes the catalytic conversion of waste PP to form carbon. Other

243 researchers have obtained similar results, that is, Mn acted as a promoter for the production of
244 CNTs in Ni-based (Ran et al., 2014; Zein and Mohamed, 2004) and Co-based catalysts (Becker
245 et al., 2011).
246   The yield of amorphous and filamentous carbons are determined by the TGA-TPO curves
247 according to their different oxidation temperatures/thermal stabilities. The carbon yield of
248 amorphous and filamentous carbons for each catalyst is obtained according to Eq.(3). This is
249 calculated based on the weight loss of each reacted catalysts on TGA-TPO results as shown in
250 Fig. 4. And the calculation results are shown in Fig. 5(a).

251
$$m_i = \frac{w_i}{M} \times 100\% \qquad (3)$$

252   Where 'i' means amorphous or filamentous carbons. The 'w_i' represents the weight of
253 amorphous or filamentous carbons deposited on the surface of reacted, 'M' represents the mass
254 of reacted catalyst, and 'm_i' means the yield of amorphous or filamentous carbons, respectively.
255 **Fig. 4.** TGA-TPO (a) and DTG-TPO (b) patterns of reacted catalyst with different amount of

(a)   (b)
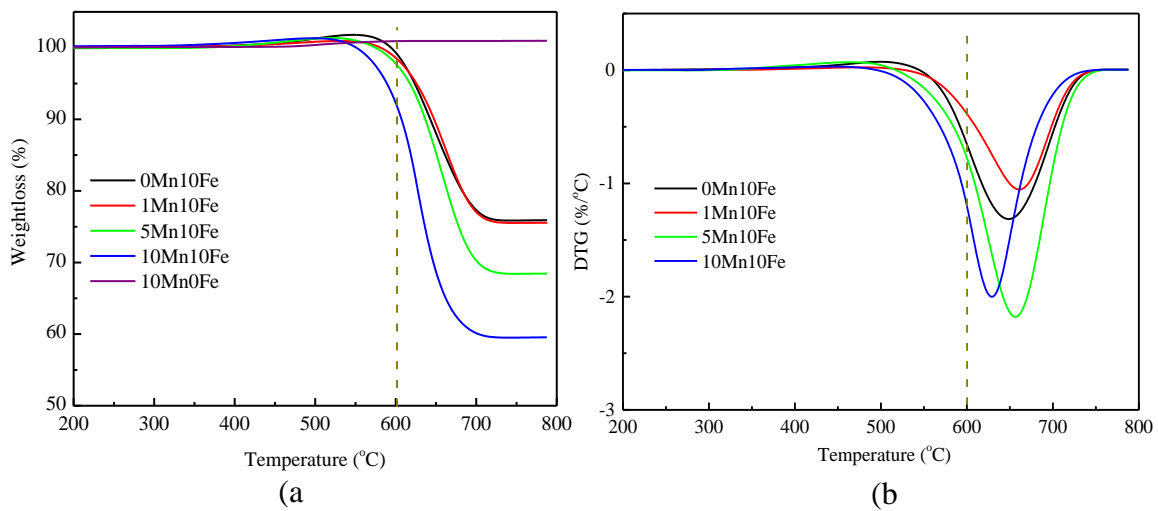
256 Mn addition in the catalysts (0Mn10Fe, 1MnFe, 5Mn10Fe, 10Mn10Fe and 10Mn0Fe).
257
258   As shown in Fig. 5(a), the addition of 1 wt.% of Mn into Fe-based catalyst shows slight
259 increase on carbon content. A further increase of Mn to 5 wt.% and 10 wt.% results in a
260 significantly incrase of both amorphous and filamentous carbons. It is worth noting that when
261 the Mn content is increased from 1 wt.% to 5 wt.%, the yield of filamentous carbons
262 significantly increases by ~6 wt.%. However, as shown in Fig. 5, when the Mn content is further
263 increased from 5 wt.% to 10 wt.%, the yield of filamentous carbon is only increased by ~2.5
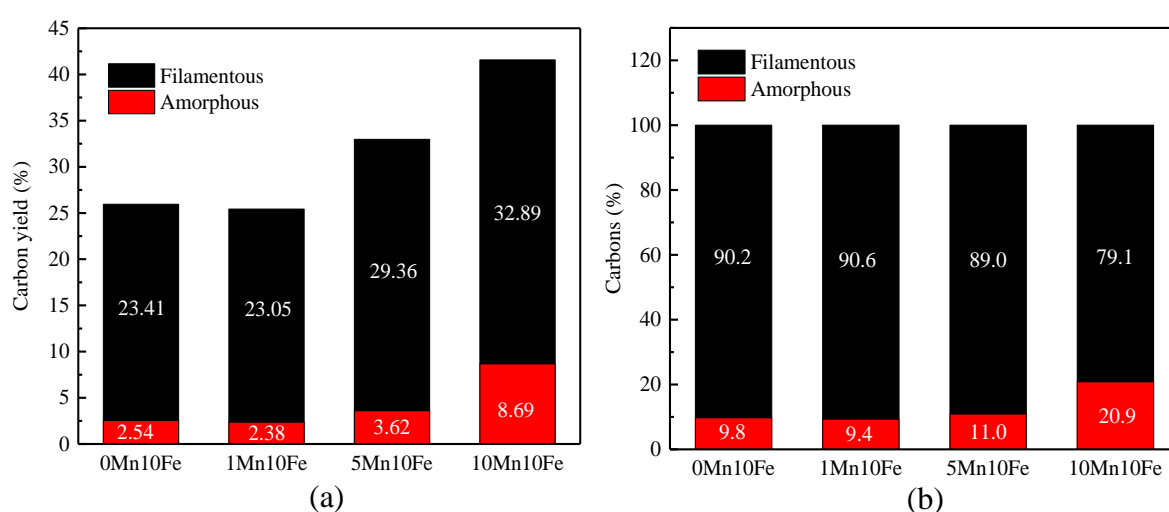264 wt.% while amorphous carbon increases by ~5 wt.%.
265   The mass ratio between amorphous and filamentous carbons for different catalysts is
266 calculated according to Eq.(4) based on the carbon yield calculated from Eq.(3), and the
267 calculation results are shown in Fig. 5(b).

268
$$M_i(\%) = \frac{m_i}{\sum m_i} \times 100\% \qquad (4)$$

269   Where the 'M_i' mean the mass ratio of filamentous and amorphous carbon.
270   As shown in Fig. 5(b), the mass ratios of amorphous and filamentous carbons generated on
271 the 0Mn10Fe, 1Mn10Fe and 5Mn10Fe catalysts are similar. However, when the Mn content

reaches 10 wt.%, the mass ratio of unwanted amorphous carbons is significantly increased to 20.9 wt.%. Although increasing the addition of Mn from 0-10 wt.% promotes carbon formation for both filamentous and armophous carbons as shown in Fig. 5(a), to some extent, the influence of Mn addition on the mass ratio of filamentous and armophous carbons is different. The addition of Mn in the range of 0-5 wt.% shows less influence on the mass ratio of produced filamentous carbons while a further addition of Mn to 10 wt.% dramastically reduces the mass ratio of filamentous carbons. It is suggested that the addition of Mn in the range of 0-5 wt.% promotes CNTs growth and the further increase of Mn content favours the formation of amorphous carbons. In addition, the DTG-TPO results in Fig.4(b) show that the oxidation peak for the 10Mn10Fe catalyst occures at lower temperature compared to 0Mn10Fe, 1Mn10Fe and 5Mn10Fe. It is indicated that a lower oxidation peak is corresponding to a higher mass ratio of amorphous carbons.


Fig. 5. (a) Amorphous/filamentous carbon yield on each of the reacted catalysts. (b) Mass ratio of amorphous and filamentous carbons on each catalyst.

3.2.2 X-ray diffraction (XRD) of reacted catalysts

Fig. 6 shows the XRD patterns of the four reacted catalysts. The Fe crystallite size is obtained from Scherrer equation. The results show that the Fe crystallite size of the four reacted catalysts is quite similar, which are 14.5 nm, 19.9 nm, 19.9 nm, and 19.9 nm for the 0Mn10Fe, 1Mn10Fe, 5Mn10Fe and 10Mn10Fe catalyst, respectively. From Fig. 6, it can be seen that the four reacted catalysts mainly contain iron carbides (Fe_3C and Fe_5C_2) and Fe phases after reaction, suggesting that α-Fe_2O_3 was fully reduced to Fe by the generated gas and then the reduced Fe was partially carbonised. Similar phase transformation of α-Fe_2O_3 to Fe_3C was also reported in the recent study (Zhang et al., 2020). For the 5Mn10Fe and 10Mn10Fe catalysts, there are additional peaks detected in the XRD patterns, indicating the existence of MnO phase. In addition, the peak intensity of Fe_3C phase is decreased while the Fe_5C_2 intensity is increased with the increase of Mn content in the Fe-based catalyst. It is suggested that Mn in the catalyst promote the carburization of Fe_5C_2 rather than Fe_3C, hence, the carbon solubility per iron atom is reduced. Similary effects on hidering the carburization of Fe have also been reported (Lee et

301 al., 1991; Nasser et al., 2018; Xu et al., 2013b). The lower carbon content accelerated
302 intermediate carbides to reach the carbon concentration required for graphite precipitation,
303 hence to promote CNTs growth (Deck and Vecchio, 2006).
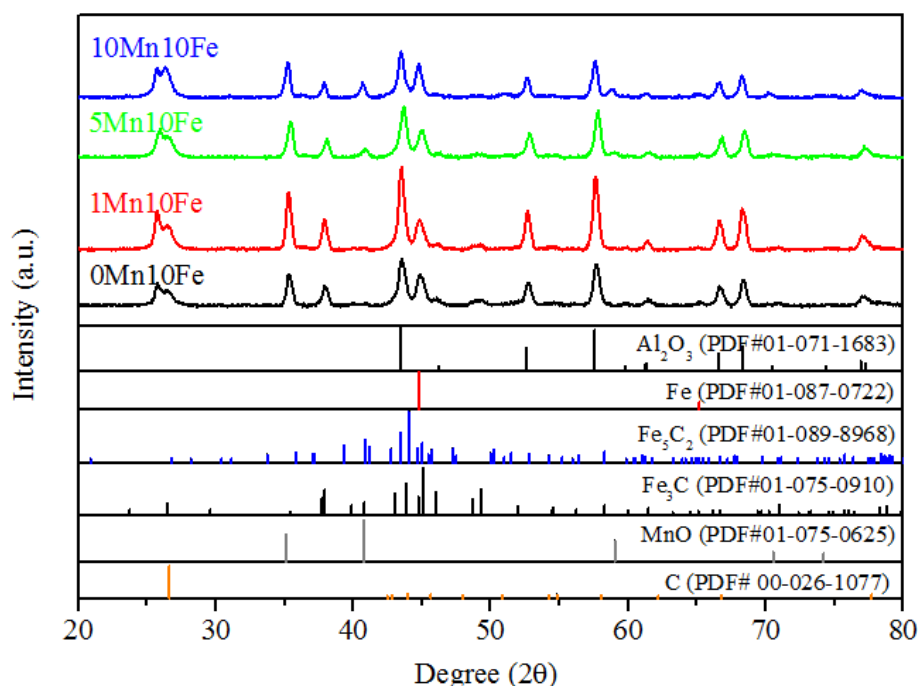
304

305 **Fig. 6.** X-ray diffraction of the reacted Fe-based catalysts contain Mn.

3.2.3 SEM and TEM results of the catalysts

307 Fig. 7 shows the SEM results of the four fresh and reacted catalysts. It is indicated that the
308 overall particle of the fresh catalyst is around 10 μm. After catalytic conversion of waste
309 plastics, an aboundance of filamentous carbons could be clearly observed on the catalysts
310 surface. The morphologies of the formed filamentous carbons on the four reacted catalysts were
311 further investigated by TEM as shown in Fig. 8. The results illustrate the filamentous carbons
312 with different structures in terms of size and homogenousness are formed over the four catalysts.
313 Obviously, the metal particles are wrapped inside the tip of the CNTs, which is consistent with
314 the tip growth mechanism of CNTs (Amelinckx et al., 1994). The formed CNTs with
315 comparatively unsmooth and unhomogeneous structures are clearly observed for the 5Mn10Fe
316 and 10Mn10Fe catalysts. The CNTs produced by the four catalysts have similar inner diameters
317 (between 10-25 nm), which is consistent with the crystallite size of the active metal particles
318 (15-20 nm) within the catalysts calculated from XRD results. It is demonstrated that the size of
319 the CNTs is directly correlated to the particle size of active sites (Kotov et al., 2019)(Cheung
320 et al., 2002; Ding et al., 2004; Nerushev et al., 2003). Interestingly, adding Mn to Fe-based
321 catalysts seems to improve the radical growth of CNTs. As shown in Fig.8, the outer diameters
322 of CNTs produced by the 0Mn10Fe and 1Mn10Fe catalysts are similar, ranging from 15-60 nm,
323 while the outer diameter of CNTs formed on 5Mn10Fe and 10Mn10Fe catalysts are larger (30-
324 115 nm). This may be attributed to the Mn contents affected the supersaturation degree of
325 carbon atoms in the Fe nanoparticle as described in a recent study (Hayashi and Kohno, 2020).
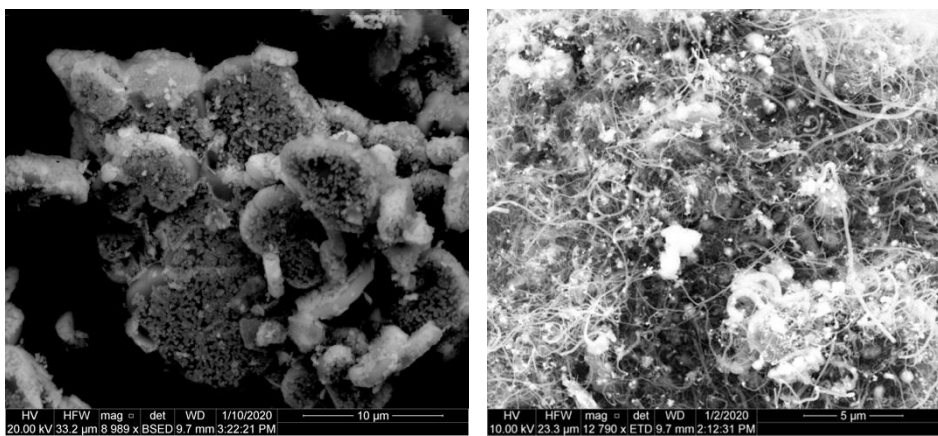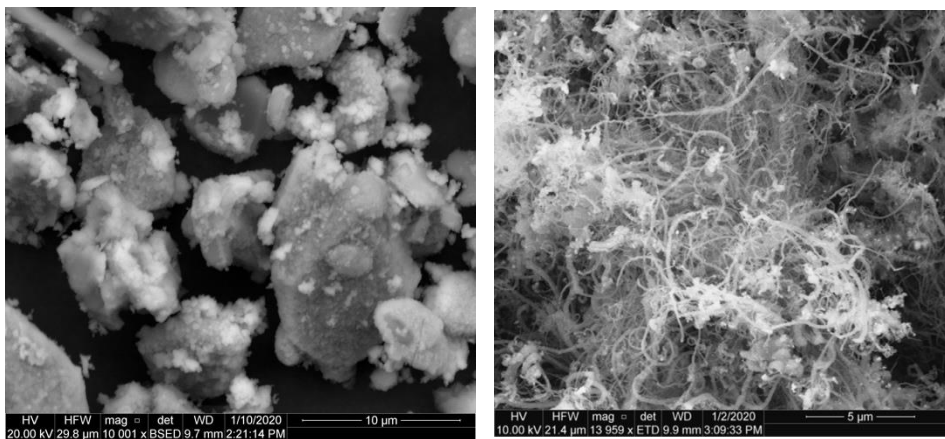
326

327

328
329   (a)0Mn10Fe

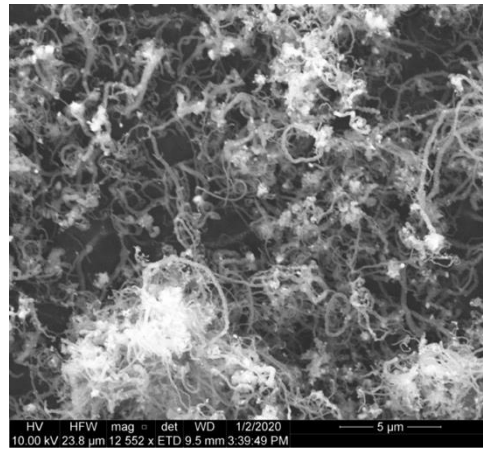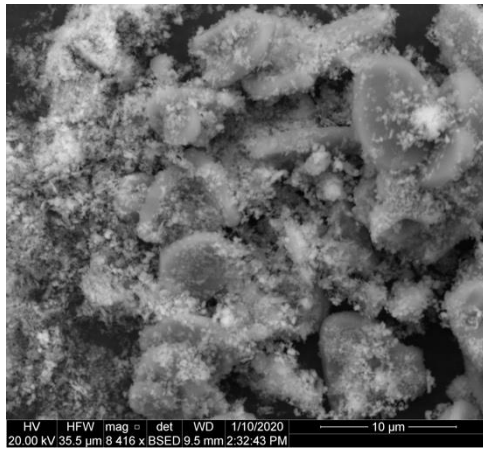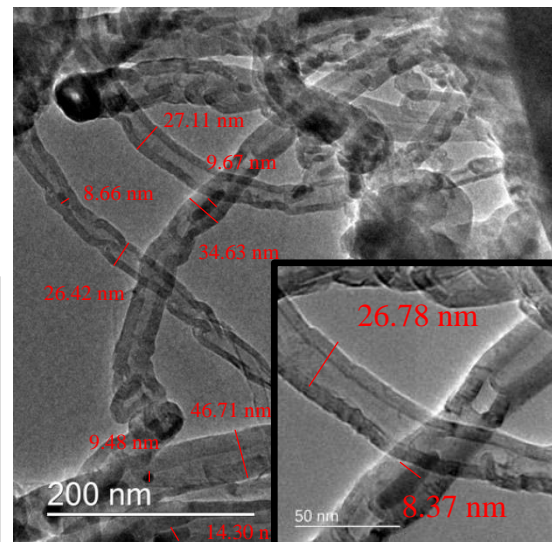330   (b)1Mn10Fe

331
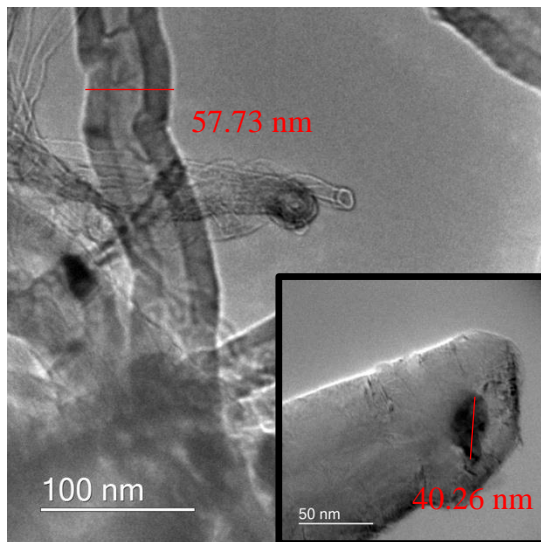332   (c) 5Mn10Fe

333
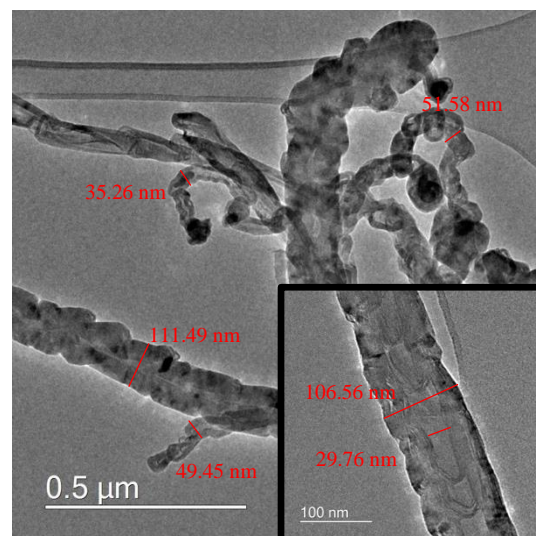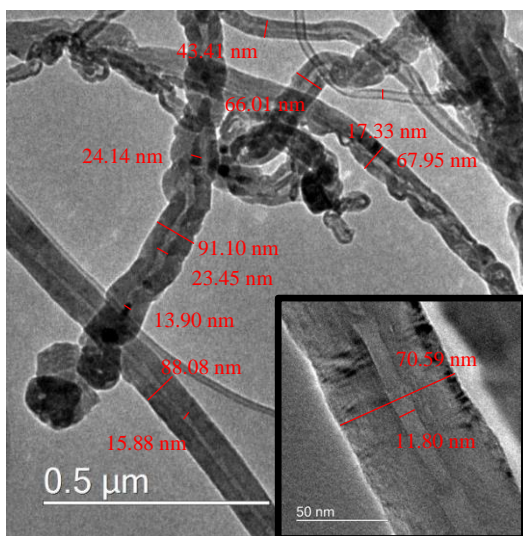334   (d) 10Mn10Fe
335 **Fig. 7.** SEM morphology analysis of the fresh (left) and reacted (right) Mn containing Fe-based
336 catalysts: (a) 0Mn10Fe (b) 1Mn10Fe, (c) 5Mn10Fe and (d) 10Mn10Fe.
337

338   (a) 0Mn10Fe   (b) 1Mn10Fe

Fig. 8. TEM of the carbon deposition on the reacted Mn containing Fe-based catalysts: (a) 0Mn10Fe (b) 1Mn10Fe, (c) 5Mn10Fe and (d) 10Mn10Fe.

3.2.4 Raman spectra of the reacted catalysts

Raman spectroscopy analysis was performed to characterise the structure of amorphous and/or graphitic carbon and estimate the purity of CNTs (DiLeo et al., 2007; Ferrari and Robertson, 2004). As shown in Fig.9, the Raman spectrum at wavelength of 1000-3000 cm^{-1} are presented to compare the carbons produced from the four Fe-based catalysts with varied Mn contents from 0-10wt.%. The Raman spectra are dominated by three vibration bands characteristic of the Raman vibrations of carbonaceous materials: the D band at ~1345 cm^{-1} arises from amorphous carbon or disordered carbon within structural defects; the G band at ~1573 cm^{-1} arises from the sp^2 stretching vibration of the graphitic structures and is characteristic of graphitic samples; and the G' band at ~2680 cm^{-1} arises from the second-order scattering process of two phonons, indicating the purity of carbons (Dresselhaus et al., 2005; Saito et al., 2003). The I_D/I_G ratio obtained by the normalizing the intensity of the D band to the G band could be used to evaluate the graphitization of carbons. As shown in Fig. 8, as the Mn content increases from 0 wt.% to 10 wt.%, the carbon I_D/I_G ratio decreases from 0.60 to 0.40, suggesting that a higher amount of Mn doping could lead to a higher ratio of graphitic carbons. The $I_{G'}/I_G$ ratio could be used to estimate the purity of CNTs (DiLeo et al., 2007). The $I_{G'}/I_G$ ratios for 0Mn10Fe, 1Mn10Fe and 5Mn10Fe are in a similar range, which indicates that the purity of the CNTs produced by the three catalysts is similar. The smallest $I_{G'}/I_G$ ratios for the 10Mn10Fe catalyst at 0.46 correspondes to the lowest purity of CNTs, which is aggreement with the TPO results shown in Fig. 5(b). Therefore, when the addition of Mn in the catalyst is below 10 wt.%, the graphitization of the produced carbon could be improved. However when excessive Mn (10 wt.%) is added into the iron-based catalyst, the purity of the produced carbon could be reduced.

Table 1 shows the comparison of our work with other different Fe-based catalyst in literatures. The detailed carbon yield, as well as the morphology and quality of produced CNTs are presented. It is indicated that 10Mn10Fe produces a high yield of carbons in comparing with other works. In addition, a large portion of the generated gases were trapped in condensation system before passing through the second stage of reactor, which decreases the carbon feedstock for CNTs growth, thus, could decrease the 10Mn10Fe catalyst capacity to produce the highest carbon yield. The excellent catalytic performance could be partially attributed to the addition of Mn. In addition, the CNTs grow on 10Mn10Fe catalyst have the lowest I_D/I_G ratio value, indicating that the produced CNTs are better graphitized than other catalysts. This could be also partially attributed to the promoting graphitization of Mn in the Fe-based catalysts.
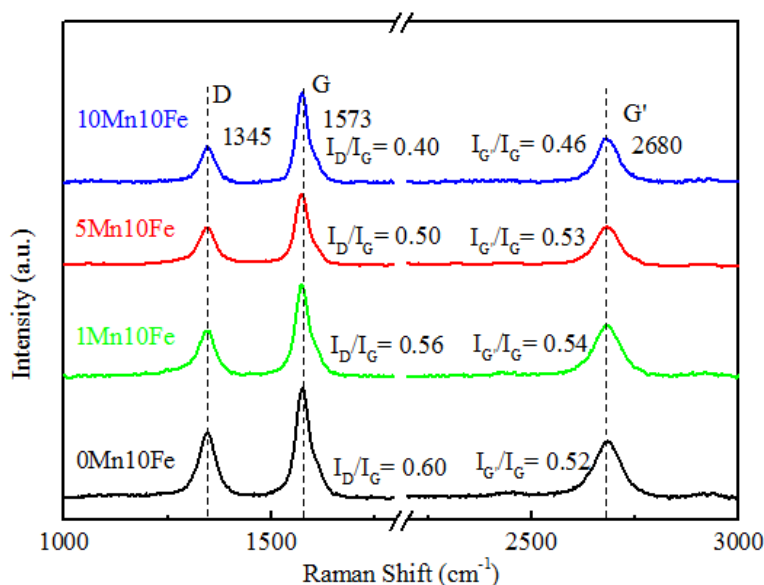
375

Fig. 9. Raman spectra of reacted catalysts.

Table 1

Comparison of carbon yield and Raman results between our research results and reports in literatures.

Feedstock	Catalyst	Carbon yield (wt.%) [a]	I_D/I_G	Ref.
PP	10Mn10Fe	41.5	0.4	This work
LDPE	Fe/Al_2O_3	34.2	0.51	(Acomb et al., 2016)
Waste tires	Fe/Al_2O_3	21.9	0.89	(Zhang et al., 2015)
PP	Fe/Cordierte	3	-	(Wang et al., 2019)
Realworld plastics	$Fe/\square-Al_2O_3$	41.3	0.64	(Yao et al., 2018b)
	$Fe/\square-Al_2O_3$	39.5	0.62	
PP	Fe/SiO_2-S	39.4	-	(Wu et al., 2017a)
	Fe/SiO_2-L	42.0	-	

[a] Obtained from the recalculation of carbon yield reported from temperature programme oxidation analysis.

Conclusion

In this study, the addition of Mn into Fe-based catalysts with content at 0 wt.%, 1wt.%, 5 wt.% and 10 wt.% have been investigated for catalytic pyrolysis of PP into CNTs. Mn is an effective promoter in the Fe-based catalyst for CNTs growth from catalytic pyrolysis of PP. The enhanced metal-support interactions by Mn addition leads to a higher yield of carbons. The dispersion of iron nanoparticles is also enhanced by Mn, inhibiting the sintering of iron particles.

In addition, the iron oxide phase is stabilized by Mn addition, therefore contributing to the stability of catalytic Fe sites. Meanwhile, the catalyst with higher Mn content favours the formation of carbides at lower carbon concentration which promotes graphite precipitation from carbides intermediates. Owing to these effects, the yield and graphitization degree of the produced CNTs increases as Mn loading increases. However, the increased Mn loading in Fe-based catalyst has negative influence on the purity of produced CNTs. Although the 10Mn10Fe catalyst produces the highest carbon yield (41.58 wt.%) than other catalysts, the mass ratio of CNTs is much lower than the 5Mn10Fe catalyst.

Acknowledgment

References

Acomb, J.C., Wu, C., Williams, P.T., 2016. The use of different metal catalysts for the simultaneous production of carbon nanotubes and hydrogen from pyrolysis of plastic feedstocks. Appl. Catal. B Environ. 180, 497–510. https://doi.org/10.1016/j.apcatb.2015.06.054

Amelinckx, S., Zhang, X.B., Bernaerts, D., Zhang, X.F., Ivanov, V., Nagy, J.B., 1994. A Formation Mechanism for Catalytically Grown Helix-Shaped Graphite Nanotubes. Science (80-.). 265, 635–639. https://doi.org/10.1126/science.265.5172.635

Andrews, R., Jacques, D., Qian, D., Rantell, T., 2002. Multiwall carbon nanotubes: Synthesis and application. Acc. Chem. Res. 35, 1008–17. https://doi.org/10.1021/ar010151m

Becker, M.J., Xia, W., Tessonnier, J.P., Blume, R., Yao, L., Schlögl, R., Muhler, M., 2011. Optimizing the synthesis of cobalt-based catalysts for the selective growth of multiwalled carbon nanotubes under industrially relevant conditions. Carbon N. Y. 49, 5253–5264. https://doi.org/10.1016/j.carbon.2011.07.043

Bezemer, G.L., Radstake, P.B., Falke, U., Oosterbeek, H., Kuipers, H.P.C.E., Van Dillen, A.J., De Jong, K.P., 2006. Investigation of promoter effects of manganese oxide on carbon nanofiber-supported cobalt catalysts for Fischer-Tropsch synthesis. J. Catal. 237, 152–161. https://doi.org/10.1016/j.jcat.2005.10.031

Bianco, A., Kostarelos, K., Prato, M., 2005. Applications of carbon nanotubes in drug delivery. Curr. Opin. Chem. Biol. 9, 674–679. https://doi.org/10.1016/j.cbpa.2005.10.005

Cheung, C.L., Kurtz, A., Park, H., Lieber, C.M., 2002. Diameter-controlled synthesis of carbon nanotubes. J. Phys. Chem. B 106, 2429–2433. https://doi.org/10.1021/jp0142278

Deck, C.P., Vecchio, K., 2006. Prediction of carbon nanotube growth success by the analysis

424 of carbon-catalyst binary phase diagrams. Carbon N. Y. 44, 267–275.
425 https://doi.org/10.1016/j.carbon.2005.07.023

426 DiLeo, R.A., Landi, B.J., Raffaelle, R.P., 2007. Purity assessment of multiwalled carbon
427 nanotubes by Raman spectroscopy. J. Appl. Phys. 101. https://doi.org/10.1063/1.2712152

428 Ding, F., Rosén, A., Bolton, K., 2004. Molecular dynamics study of the catalyst particle size
429 dependence on carbon nanotube growth. J. Chem. Phys. 121, 2775–2779.
430 https://doi.org/10.1063/1.1770424

431 Ding, M., Qiu, M., Liu, J., Li, Y., Wang, T., Ma, L., Wu, C., 2013. Influence of manganese
432 promoter on co-precipitated Fe-Cu based catalysts for higher alcohols synthesis. Fuel 109, 21–
433 27. https://doi.org/10.1016/j.fuel.2012.06.034

434 Dresselhaus, M.S., Dresselhaus, G., Saito, R., Jorio, A., 2005. Raman spectroscopy of carbon
435 nanotubes. Phys. Rep. 409, 47–99. https://doi.org/10.1016/j.physrep.2004.10.006

436 Drzyzga, O., Prieto, A., 2019. Plastic waste management, a matter for the 'community.' Microb.
437 Biotechnol. 12, 66–68. https://doi.org/10.1111/1751-7915.13328

438 Ferrari, A.C., Robertson, J., 2004. Raman spectroscopy of amorphous, nanostructured,
439 diamond-like carbon, and nanodiamond. Philos. Trans. R. Soc. A Math. Phys. Eng. Sci. 362,
440 2477–2512. https://doi.org/10.1098/rsta.2004.1452

441 Feyzi, M., Jafari, F., 2012. Study on iron-manganese catalysts for Fischer-Tropsch synthesis.
442 Ranliao Huaxue Xuebao/Journal Fuel Chem. Technol. 40, 550–557.
443 https://doi.org/10.1016/s1872-5813(12)60021-8

444 Hayashi, T., Kohno, H., 2020. Diameter-Modulated Multi-Walled Carbon Nanotubes Without
445 Bamboo-Like Partitions: Growth, Structure and Deformation Behaviors. J. Nanosci.
446 Nanotechnol. 20, 3038–3041. https://doi.org/https://doi.org/10.1166/jnn.2020.17451

447 He, M., Fedotov, P. V., Chernov, A., Obraztsova, E.D., Jiang, H., Wei, N., Cui, H., Sainio, J.,
448 Zhang, W., Jin, H., Karppinen, M., Kauppinen, E.I., Loiseau, A., 2016. Chiral-selective growth
449 of single-walled carbon nanotubes on Fe-based catalysts using CO as carbon source. Carbon N.
450 Y. 108, 521–528. https://doi.org/10.1016/j.carbon.2016.07.048

451 Iijima, S., 1991. Helical microtubules of graphitic carbon. Nature 354, 56–58.
452 https://doi.org/https://doi.org/10.1038/354056a0

453 Jia, J., Zhang, P., Chen, L., 2016. The effect of morphology of α-MnO2 on catalytic
454 decomposition of gaseous ozone. Catal. Sci. Technol. 6, 5841–5847.
455 https://doi.org/10.1039/c6cy00301j

456 Karásková, K., Obalová, L., Jirátová, K., Kovanda, F., 2010. Effect of promoters in Co-Mn-Al
457 mixed oxide catalyst on N2O decomposition. Chem. Eng. J. 160, 480–487.
458 https://doi.org/10.1016/j.cej.2010.03.058

459   Kotov, V., Sviatenko, A., Nebesnyi, A., Filonenko, D., Khovavko, A., Bondarenko, B., 2019.
460   CNTs growth on reduced iron. Mater. Today Proc. https://doi.org/10.1016/j.matpr.2019.11.287

461   Landi, B.J., Ganter, M.J., Cress, C.D., DiLeo, R.A., Raffaelle, R.P., 2009. Carbon nanotubes
462   for lithium ion batteries. Energy Environ. Sci. 2, 638–654. https://doi.org/10.1039/b904116h

463   Lebreton, L., Andrady, A., 2019. Future scenarios of global plastic waste generation and
464   disposal. Palgrave Commun. 5, 1–11. https://doi.org/10.1057/s41599-018-0212-7

465   Lee, M.D., Lee, J.F., Chang, C.S., Dong, T.Y., 1991. Effects of addition of chromium,
466   manganese, or molybdenum to iron catalysts for carbon dioxide hydrogenation. Appl. Catal.
467   72, 267–281. https://doi.org/10.1016/0166-9834(91)85055-Z

468   Leith, I.R., Howden, M.G., 1988. Temperature-programmed reduction of mixed iron-
469   manganese oxide catalysts in hydrogen and carbon monoxide. Appl. Catal. 37, 75–92.
470   https://doi.org/10.1016/S0166-9834(00)80752-6

471   Lettieri, P., Al-Salem, S.M., 2011. Thermochemical Treatment of Plastic Solid Waste, Waste.
472   Elsevier Inc. https://doi.org/10.1016/B978-0-12-381475-3.10017-8

473   Lin, J., Yang, Yihang, Zhang, H., Li, F., Yang, Yulin, 2020. Carbon nanotube growth on
474   titanium boride powder by chemical vapor deposition: Influence of nickel catalyst and carbon
475   precursor   supply.   Ceram.   Int.   46,   12409–12415.
476   https://doi.org/10.1016/j.ceramint.2020.02.002

477   Liu, Y., Qian, W., Zhang, Q., Ning, G., Luo, G., Wang, Y., Wang, D., Wei, F., 2009. Synthesis
478   of high-quality, double-walled carbon nanotubes in a fluidized bed reactor. Chem. Eng.
479   Technol. 32, 73–79. https://doi.org/10.1002/ceat.200800298

480   Modekwe, H.U., Mamo, M., Moothi, K., Daramola, M.O., 2020. Synthesis of bimetallic
481   NiMo/MgO catalyst for catalytic conversion of waste plastics (polypropylene) to carbon
482   nanotubes (CNTs) via chemical vapour deposition method. Mater. Today Proc.
483   https://doi.org/10.1016/j.matpr.2020.02.398

484   Nahil, M.A., Wu, C., Williams, P.T., 2015. Influence of metal addition to Ni-based catalysts
485   for the co-production of carbon nanotubes and hydrogen from the thermal processing of waste
486   polypropylene.   Fuel   Process.   Technol.   130,   46–53.
487   https://doi.org/10.1016/j.fuproc.2014.09.022

488   Nasser, A.H., Guo, L., Elnaggar, H., Wang, Y., Guo, X., Abdelmoneim, A., Tsubaki, N., 2018.
489   Mn-Fe nanoparticles on a reduced graphene oxide catalyst for enhanced olefin production from
490   syngas in a slurry reactor. RSC Adv. 8, 14854–14863. https://doi.org/10.1039/c8ra02193g

491   Nerushev, O.A., Dittmar, S., Morjan, R.-E., Rohmund, F., Campbell, E.E.B., 2003. Particle
492   size dependence and model for iron-catalyzed growth of carbon nanotubes by thermal chemical
493   vapor deposition. J. Appl. Phys. 93, 4185–4190. https://doi.org/10.1063/1.1559433

494   Pineau, A., Kanari, N., Gaballah, I., 2006. Kinetics of reduction of iron oxides by H2. Part I:
495   Low temperature reduction of hematite. Thermochim. Acta 447, 89–100.
496   https://doi.org/10.1016/j.tca.2005.10.004

497   Ran, M., Chu, W., Liu, Y., Liu, D., Zhang, C., Zheng, J., 2014. Doping effects of manganese
498   on the catalytic performance and structure of NiMgO catalysts for controllabe synthesis of
499   multi-walled carbon nanotubes. J. Energy Chem. 23, 781–788. https://doi.org/10.1016/S2095-
500   4956(14)60212-6

501   Saito, R., Grüneis, A., Samsonidze, G.G., Brar, V.W., Dresselhaus, G., Dresselhaus, M.S., Jorio,
502   A., Cançado, L.G., Fantini, C., Pimenta, M.A., Souza Filho, A.G., 2003. Double resonance
503   Raman spectroscopy of single-wall carbon nanotubes. New J. Phys. 5.
504   https://doi.org/10.1088/1367-2630/5/1/157

505   Shah, K.A., Tali, B.A., 2016. Synthesis of carbon nanotubes by catalytic chemical vapour
506   deposition: A review on carbon sources, catalysts and substrates. Mater. Sci. Semicond. Process.
507   41, 67–82. https://doi.org/10.1016/j.mssp.2015.08.013

508   Sivakumar, V.M., Abdullah, A.Z., Mohamed, A.R., Chai, S.P., 2011. Optimized parameters for
509   carbon nanotubes synthesis over Fe and Ni catalysts VIA methane CVD. Rev. Adv. Mater. Sci.
510   27, 25–30.

511   Tang, W., Wu, X., Li, D., Wang, Z., Liu, G., Liu, H., Chen, Y., 2014. Oxalate route for
512   promoting activity of manganese oxide catalysts in total VOCs' oxidation: Effect of calcination
513   temperature and preparation method. J. Mater. Chem. A 2, 2544–2554.
514   https://doi.org/10.1039/c3ta13847j

515   Wang, J., Shen, B., Lan, M., Kang, D., Wu, C., 2019. Carbon nanotubes (CNTs) production
516   from catalytic pyrolysis of waste plastics: The influence of catalyst and reaction pressure. Catal.
517   Today 1–8. https://doi.org/10.1016/j.cattod.2019.01.058

518   Wu, C., Liu, X., Williams, P.T., Nahil, M.A., Zhang, Y., 2017a. Development of Ni- and Fe-
519   based catalysts with different metal particle sizes for the production of carbon nanotubes and
520   hydrogen from thermo-chemical conversion of waste plastics. J. Anal. Appl. Pyrolysis 125, 32–
521   39. https://doi.org/10.1016/j.jaap.2017.05.001

522   Wu, C., Nahil, M.A., Miskolczi, N., Huang, J., Williams, P.T., Engineering, P., Ls, L., 2017b.
523   Production and application of carbon nanotubes , as a co-product of hydrogen from the
524   pyrolysis-catalytic reforming of waste plastic. Process Saf. Environ. Prot. 103, 107–114.
525   https://doi.org/10.1016/j.psep.2016.07.001

526   Wu, C., Williams, P.T., 2009. Hydrogen production from the pyrolysis-gasification of
527   polypropylene: Influence of steam flow rate, carrier gas flow rate and gasification temperature.
528   Energy and Fuels 23, 5055–5061. https://doi.org/10.1021/ef900278w

529   Xu, J.D., Zhu, K.T., Weng, X.F., Weng, W.Z., Huang, C.J., Wan, H.L., 2013a. Carbon
530   nanotube-supported Fe-Mn nanoparticles: A model catalyst for direct conversion of syngas to

531   lower olefins. Catal. Today 215, 86–94. https://doi.org/10.1016/j.cattod.2013.04.018

532   Xu, J.D., Zhu, K.T., Weng, X.F., Weng, W.Z., Huang, C.J., Wan, H.L., 2013b. Carbon
533   nanotube-supported Fe-Mn nanoparticles: A model catalyst for direct conversion of syngas to
534   lower olefins. Catal. Today 215, 86–94. https://doi.org/10.1016/j.cattod.2013.04.018

535   Yan, Y., Miao, J., Yang, Z., Xiao, F.X., Yang, H. Bin, Liu, B., Yang, Y., 2015. Carbon nanotube
536   catalysts: Recent advances in synthesis, characterization and applications. Chem. Soc. Rev. 44,
537   3295–3346. https://doi.org/10.1039/c4cs00492b

538   Yang, R.X., Chuang, K.H., Wey, M.Y., 2015. Effects of Nickel Species on Ni/Al2O3 Catalysts
539   in Carbon Nanotube and Hydrogen Production by Waste Plastic Gasification: Bench- and Pilot-
540   Scale Tests. Energy and Fuels 29, 8178–8187. https://doi.org/10.1021/acs.energyfuels.5b01866

541   Yang, Y., Xiang, H.W., Tian, L., Wang, H., Zhang, C.H., Tao, Z.C., Xu, Y.Y., Zhong, B., Li,
542   Y.W., 2005. Structure and Fischer-Tropsch performance of iron-manganese catalyst
543   incorporated with SiO2. Appl. Catal. A Gen. 284, 105–122.
544   https://doi.org/10.1016/j.apcata.2005.01.025

545   Yang, Y., Xiang, H.W., Xu, Y.Y., Bai, L., Li, Y.W., 2004. Effect of potassium promoter on
546   precipitated iron-manganese catalyst for Fischer-Tropsch synthesis. Appl. Catal. A Gen. 266,
547   181–194. https://doi.org/10.1016/j.apcata.2004.02.018

548   Yao, D., Zhang, Y., Williams, P.T., Yang, H., Chen, H., 2018. Co-production of hydrogen and
549   carbon nanotubes from real-world waste plastics: Influence of catalyst composition and
550   operational parameters. Appl. Catal. B Environ. 221, 584–597.
551   https://doi.org/10.1016/j.apcatb.2017.09.035

552   Zein, S.H.S., Mohamed, A.R., 2004. Mn/Ni/TiO2 catalyst for the production of hydrogen and
553   carbon nanotubes from methane decomposition. Energy and Fuels 18, 1336–1345.
554   https://doi.org/10.1021/ef0340864

555   Zghal, S., Jedidi, I., Cretin, M., Cerneaux, S., Abdelmouleh, M., 2020. One-step synthesis of
556   highly porous carbon graphite/carbon nanotubes composite by in-situ growth of carbon
557   nanotubes for the removal of humic acid and copper (II) from wastewater. Diam. Relat. Mater.
558   101, 107557. https://doi.org/10.1016/j.diamond.2019.107557

559   Zhang, T., Wang, Q., Lv, X., Luo, Y., Zhang, Y., 2020. Transformation of primary siderite
560   during coal catalytic pyrolysis and its effects on the growth of carbon nanotubes. Fuel Process.
561   Technol. 198, 106235. https://doi.org/10.1016/j.fuproc.2019.106235

562   Zhang, Y., Nahil, M.A., Wu, C., Williams, P.T., 2017. Pyrolysis–catalysis of waste plastic
563   using a nickel–stainless-steel mesh catalyst for high-value carbon products. Environ. Technol.
564   (United Kingdom) 38, 2889–2897. https://doi.org/10.1080/09593330.2017.1281351

565   Zhang, Y., Wu, C., Nahil, M.A., Williams, P., 2015. Pyrolysis-catalytic reforming/gasification
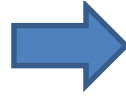566   of waste tires for production of carbon nanotubes and hydrogen. Energy and Fuels 29, 3328–

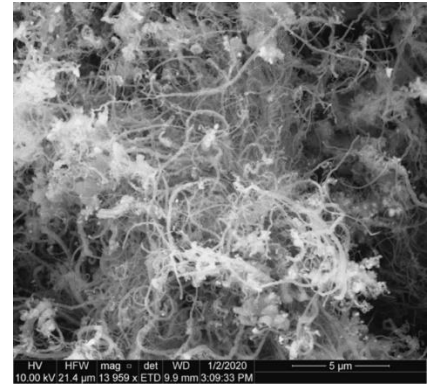567   3334. https://doi.org/10.1021/acs.energyfuels.5b00408

568   Zhao, A., Ying, W., Zhang, H., Hongfang, M., Fang, D., 2012. Ni/Al 2O 3 catalysts for syngas
569   methanation: Effect of Mn promoter. J. Nat. Gas Chem. 21, 170–177.
570   https://doi.org/10.1016/S1003-9953(11)60350-2

Graphical abstract

Fe/Al$_2$O$_3$

Mn doping

Novelties

This work contributes to the enhancement of carbon nanotubes production from waste plastics using Fe/Al_2O_3 by doping Mn promoter. The addition of Mn has been optimised related to the quality of CNTs (e.g. yield and ratio of filamentous carbons). The work finds that the manipulation of intermediate carbides during the CNTs formation from waste plastics is very important and a key influence of Mn on catalyst is to modify the interaction between Fe and Al_2O_3 which can be optimised for CNTs formation. The work provides a novel catalyst formation for waste plastics management for high value CNTs production.

Highlights

- Mn is effective to promote Fe-catalyst for CNTs production
- An optimal content of Mn is required for CNTs formation
- Fe-metal and Al_2O_3 support interactions can be promoted by Mn addition
- Formation of intermediate carbides can be promoted with Mn addition

Su He: Carry out major experimental work, Writing- Original draft preparation. **Yikai Xu & Steven Bell**: Methodology and SEM and Raman analysis. **Yeshui Zhang**: Methodology and TEM analysis. **Chunfei Wu:** Conceptualization, Methodology, Editing.

Declaration of interests

☒ The authors declare that they have no known competing financial interests or personal relationships that could have appeared to influence the work reported in this paper.

☐The authors declare the following financial interests/personal relationships which may be considered as potential competing interests:

Abstract

Thermo-chemical conversion is a promising technology for the recycle of waste plastics, as it can produce high-value products such as carbon nanotubes (CNTs) and hydrogen. However, the low yield of CNTs is one of the challenges. In this work, the addition of Mn (0 wt.%, 1 wt.%, 5 wt.%, and 10 wt.%) to Fe-based catalyst to improve the production of CNTs has been investigated. Results show that the increase of Mn content from 0 wt.% to 10 wt.% significantly promotes CNTs yield formed on the catalyst from 23.4 wt.% to 32.9 wt.%. The results show that Fe-particles in the fresh catalysts are between 10-25 nm. And the addition of Mn in the Fe-based catalyst enhanced the metal-support interactions and the dispersion of metal particles, thus leading to the improved catalytic performance in relation to filamentous carbon growth. In addition, the graphitization of CNTs is promoted with the increase of Mn content. Overall, in terms of the quantity and quality of the produced CNTs, 5 wt.% of Mn in Fe-based catalyst shows the best catalytic performance, due to the further increase of Mn content from 5 wt.% to 10 wt.% led to a dramatic decrease of purity by 10 wt.%.